A Review of Nonlinear Low Frequency (LF) Wave Observations in Space Plasmas: On the Development of Plasma Turbulence

Bruce T. Tsurutani
Jet Propulsion Laboratory
California Institute of Technology
4800 Oak Grove Drive
Pasadena, California 911(N U.S.A.

Karl-Heinz Glassmeier
Institut für Geophysik
Technical University of Braunschweig
D-3300" Braunschweig, Germany

and

Fritz M. Neubauer
Universitat zu Köln
Institut für Geophysik und Meteorologic
Köln 41, Germany

ABSTRACT

As the lead-off presentation for the topic of nonlinear waves and their evolution, we will illustrate some prominent examples of waves in space plasmas. We will describe recent observations detected within planetary foreshocks, near comets and in interplanetary space. It is believed that the nonlinear LF plasma wave features discussed here are part of and may be basic to the development of plasma turbulence. In this sense., this is one area of space plasma physics that is fundamental, with applications to fusion physics and astrophysics as well. It is hoped that the reader(s) will be stimulated to study nonlinear wave development themselves, if he/she is not already involved.

INTRODUCTION

One of **the most** fundamental topics in space plasma physics is the nature of nonlinear waves and their evolution to partial and full turbulence. Because of the large scale sizes of waves in space, multipoint measurements can be made within a single wavelength, as the waves get convected past/propagate past the spacecraft. Of the various wave phenomena in space plasmas, the cometary case is unique because there is a well-defined narrow-band "pump" frequency which is essentially at the local ion cyclotron frequency in the instrument (spacecraft) rest frame of reference. At frequencies higher than the "pump", the wave power falls-off with frequency dependences between $f^{-5/3}$ to $f^{-2.5}$, indicative of spectra developing towards, or reaching Kolmogorov or Kraichnan turbulence.

Detailed investigation of waves at higher and lower frequencies than the pump frequency can be used to identify "daughter" and "granddaughter" waves, and thus determine the specific mechanism for the formation of plasma turbulence. Various mechanisms such as wave-wave modulational instabilities, decay instabilities, four-wave processes, wave-particle interactions, dispersion and damping all can affect and be part of this turbulent spectrum (see Chen, 1990). To begin the review, we will first discuss the plasma instabilities that are involved at comets and planetary foreshocks. Because cometary ions initially have almost zero velocity in the spacecraft frame, ion cyclotron waves are detected at the local cyclotron frequency, making this case more tractable (although there is a finite frequency width associated with the resonance, and cyclotron harmonics may also be present, these effects are small in comparison with the broad wave spectrum found at comets). The same basic wave instabilities/modes are observed in planetary foreshocks, regions where back streaming solar wind ion beams can generate LF electromagnetic waves. In this latter case the beam is not necessarily monoenergetic, and therefore the waves are not generated at a single narrow frequency band (the pump is quite broad). Because the spacecraft is not in the same reference frame, there are also strong Doppler shifts which vary with solar wind speed variations. On the other hand, foreshock regions have been crossed hundreds of times by spacecraft, allowing large statistical studies of nonlinear wave/turbulence development. In this paper we will also examine data for passes which occur well downstream of the Earth. The reason why this is of particular interest is that waves in this region have had greater time to evolve in a temporal sense, allowing greater possibility of wave-wave interactions to occur. This will be the second topical area addressed in this review. The third and final topic will be observations of interplanetary nonlinear Alfvén waves, and possible wave phase-steepening, perhaps an initial stage in the development of heliospheric turbulence.

RESULTS

The fundamental plasma instability leading to the development of LF plasma waves discussed in this paper is illustrated in Figure 1, shown for the cometary case. As a comet approaches the sun, beating of the nuclear surface leads to sublimation of its volatile atoms and molecules (-N)% H_2O molecules). These particles attain velocities of -1 km s-1 directed radially outward from the nucleus. At 1 AU, the time scale for photoionization and charge exchange (with solar wind protons) to take place is $\sim 10^6$ s. 'I'bus, the atoms and molecules typically propagate -106 km before being ionized.

Once ionized, the ions form a narrow beam relative to the fast flowing solar wind plasma (typical radial 11ow speeds arc ~400 km S-l) and its embedded magnetic field. If the interplanetary magnetic field (IMF) is parallel to the solar wind velocity vector (top panel of Figure 1), the freshly created ions will be a beam in the plasma rest frame propagating at a velocity $-V_{SW}$ (i.e., in the direction towards the sun). If, on the other hand, the IMF is orthogonal to the solar wind flow direction as for the case illustrated in the bottom panel of the Figure, the $\vec{V} \times \vec{B}$ Lorentz force will cause the pickup of the ions, forming a narrow ring with velocity V_{SW} relative to the solar wind, and a convected velocity V_{SW} past the spacecraft. For intermediate field angles, a narrow ring-bcam distribution is formed.

All of the above three ion distributions (assuming, a sufficiently large beam density) arc unstable to resonant wave growth. Discussions of the instabilities can be found in Wu and Davidson (1972), Thorne and Tsurutani (1987), Brinca (1991), Gary (1991) and Roberts and Goldstein (1991). Thorne and Tsurutani (1987) have pictorially illustrated the cyclotron resonance conditions. Wc have adapted these schematics and present them here in Figure 2.

The uppermost panel of Figure 2 represents the case for the upper panel of Figure 1. In the plasma frame, the ion beam is propagating at a speed V_{SW} towards the sun. The magnetosonic mode phase speed for typical solar wind conditions at 1 AU is -70 km s^{-1} or - 1/S Vs$_w$. Because the left-hand ions are overtaking the right-hand waves, they sense the waves as left-handed. This is called an anomalous Doppler shift. A cyclotron resonance can occur when the resonance condition (top of Figure 2) is met.

The second panel of Figure 2 illustrates the ordinary cyclotron resonant interaction. This corresponds closely to the lower panel of Figure 1. For a predominantly orthogonal pitch angle distribution (-90"), but with some parallel velocity component, $V_{\parallel} > V_{ph}$, the ion (parallel to the

4

field) motion causes the wave to Doppler-shift up to the ion cyclotron frequency. Left-hand waves arc generated by this instability. The waves propagate in the opposite direction to the particles. This instability is basically the same as the magnetospheric loss cone instability (Kennel and Petschek, 1966). It should be noted, however, that for an exactly 90<' pitch angle distribution, the plasma distribution is stable. This is the situation for post-storm magnetospheric ring current particles, where all particles except those at -900 are strongly pitch angle scattered towards the loss cone.

Energetic electron beams or rings can also generate LF waves, but with the opposite polarization as that for ions. Because the Doppler shift of waves must be much larger than that for ions to match the gyrofrequency of the electrons, the kinetic energies for resonance are typically in the ~MeV range (compared to 1-10 keV for the ions). The electron resonance examples are shown in the bottom two panels of Figure 2.

Figure 3 illustrates the particles and waves within a planetary foreshock. in this example, the IMF makes an angle of -45" relative to the sun-planet line, the Parker spiral angle for the Earth's case at 1 AU. The field lines are tangent to the (perpendicular) shock at -02 LT and normal m the (quasi parallel) shock at -10 LT.

Particles reflected from the shock, escaping from the magnetosheath, or leaked from the magnetosphere, will travel up the magnetic field lines in a direction towards the Sun, but will be convected in the antisunward direction by the solar wind. Because the electrons have higher velocities than the ions for the same energies, their foreshock boundary is further sunward than the ion foreshock (Tsurutani and Rodriguez, 1981).

The ions (and electrons) are subject to the same instabilities as those at comets, cyclotron resonant ring-beam instabilities. The only difference is the species of the ions (protons, for bow shock-reflected and magnetosheath particles, energetic protons coming from the Earth's magnetosphere, and $S+$, S^{++} and $0+$, for Jovian magnetospheric particles). For foreshock cases, there is a spectrum of streaming velocities of the ions, and thus the wave generation is expected to occur at a variety of frequencies. Because the ions and electrons have high velocities relative to the spacecraft frame, there will be strong Doppler shifts and the waves will not be measured at the particle cyclotron frequencies.

Jovian Foreshock

Ever since the Pioneer and Voyager spacecraft have encountered the Jovian foreshock, there has been a controversy about the particle species generating the upstream waves. Since relativistic magnetospheric electrons and energetic ions and reflected solar wind protons are all present in the upstream region, it is difficult to distinguish between instabilities due to these various particles. Smith et al. (1 976) made the first measurements and speculated that the large amplitude, nonlinear, 20 min waves (see Figure 4), were generated by relativistic -McV electrons. Later, Voyager results (Smith et al., 1983, 1984; Goldstein et al., 1983; 1985; 1986; Smith and Lee, 1986) led to a variety of opinions, depending on the particular data set and emphases of the authors. So far, the above authors have made arguments for all of the above particle possibilities. Keys to the arguments have been the measured handedness of the waves in the spacecraft frame. The wave polarizations in the plasma frame were inferred from the spacecraft measurements. However, it should be noted that there have been no measurements made to date that have uniquely determined the polarization in the plasma frame. All single point triaxial magnetometer measurements only determine the polarization in the spacecraft frame. The plasma frame polarization must be deduced. Referring back to Figure 2, if the waves were detected as left-hand polarized in the spacecraft frame, that could correspond to the top panel of the Figure. The right-hand waves would be propagating toward the sun, but because their phase velocities are less than the solar wind speed, they could be anomalously Doppler shifted to appear left-hand polarized in the spacecraft frame. In this case, the right-hand polarized waves would have been generated by an ion beam propagating toward the sun. Conversely, if the waves are detected as right-hand polarized in the spacecraft frame, that would correspond to the third panel of Figure 4, left-hand polarized waves that are generated by (relativistic) electron beams propagating towards the sun. The second from the top and the bottom panels are not applicable to the foreshock case, because these correspond to large initial particle pitch angles. By definition such particles would have small parallel velocity components, and therefore cannot propagate far into the upstream region.

Some recent results of wave observations in the Jovian foreshock (Tsurutani et al., 1993) are shown in Figure 5. The Jovian foreshock waves are displayed in the SH coordinate system. In this system, $\hat{x}$ is along the spacecraft-sun line, $\hat{y}$ is in the $\dot{\Omega} \times \hat{x}$ direction, where $\hat{Q}$ is the sun's rotation (north) pole, and $\hat{z}$ completes a light-hand system. There are several significant features shown in the Figure. Tbc waves are large amplitude, with the peak-to-peak transverse components as large as $\Delta \vec{B}/|B| \sim 1$ and a compressional component $\Delta|B|/|B| \sim -0.5$. Solid horizontal bars in the $|B|$ panel indicate intervals where minimum variance analyses (Sonnerup and Cahill, 1967; Smith and Tsurutani, 1976) have been performed. The angle that $\hat{k}$ subtends relative to $\vec{B}$ is indicated

between the third and fourth panels. The labels "L" and "R" correspond to spacecraft frame left-hand and right-hand polarizations, respectively.

The interesting feature of the waves in Figure 5 is that there is a mix of both (spacecraft frame) right- and left-hand polarizations within the same wave train. The right-hand waves occur when B_x is relatively small, and the left-hand(ic(i waves when B_x is large. I'bus, this is consistent with the right-hand (spacecraft frame) wave cases occurring during intervals when the waves are propagating orthogonal to the solar wind direction and have small Doppler shifts. The left-hand waves can be right-hand in the plasma frame propagating towards the sun (when B_x is large) which have been anomalously Doppler-shifted by the solar wind. The high frequency wave packet detected at 1705 UT supports this hypothesis. The polarization is left-bancicd. Since we arc fairly certain that this is a whistler packet, this corresponds to anomalously Doppler shifted whistler mode waves. It has been concluded (Tsurutani et al., 1993) that all of these waves within the entire interval of the figure could be interpreted as being right-hand polarized in the plasma frame.

Different possible ion species were considered as the source of free energy. The energies for cyclotron resonance were calculated based on the wave properties and the assumption of generation by a sunward propagating ion beam. It was found that energetic magnetospheric heavy ion beams (S+, S++, etc.) could not be the source of the waves. The parallel velocity needed for resonance is too low for the particles to propagate into the upstream region. The calculated parallel velocities are lower than the measured solar wind speeds and thus such particles would be convected downstream. Heavy neutral particles (of magnetospheric origin) ionized in the upstream region arc a possible source, but the ambient neutral densities would have to be very large to create a beam density that would go unstable. This is because the ionization time scale is very low due to the low solar UV radiation and solar wind ion densities at such large heliospheric distances from the sun (for photoionization and charge exchange processes, respectively). This possibility can thus be eliminated. The last possibility is low energy protons. Substituting numbers into the resonance condition, Tsurutani et al. (1993) found that the resonant energy in the spacecraft frame is -2 keV. This is essentially the energy for reflected solar wind protons. Other intervals of Jovian foreshock data are presently being analyzed to see if all previously reported foreshock waves are consistent with this scenario, or if different ion and/or electron beams must be present at some times to be able to explain all of the observations.

The magnetosonic waves plus their attached whistler wave trains have interesting nonlinear features. The whistler packet amplitude decreases with distance upstream of the magnetosonic wave (Figure 5) [because the wave is propagating towards the sun while being blown back by the

solar wind, the "upstream" end of the wave, e.g., edge along the direction of propagation is detected last in time in the Figures]. Because this amplitude fall-off is linear and not exponential, it is believed that Ibis feature cannot be caused by Landau damping. Dispersion of the whistler mode components of the magnetosonic wave is a more likely possibility. The whistler and the trailing part of the magnetosonic wave are analyzed separately using the minimum variance method. The results are shown in Figures 6 a and b, respectively. B_1, B_2 and B_3 correspond to the field components in the maximum, intermediate and minimum variance directions and λ_1, λ_2 and λ_3, the corresponding eigen values. In panel 6a, we find that the whistler packet has a maximum peak-to-peak amplitude of -1.0 nT in a -0.5 nT field, or a $|\Delta|\vec{B}|/|B|$ value -2.0. The wave has circular polarization and is plane polarized ($\lambda_2/\lambda_3 = 28.0$). It is propagating at a large (-30") angle relative to the upstream ambient magnetic field. The trailing portion of the wave is shown in panel 6b. For the two minute interval (1702-1704 UT) of this part of the magnetosonic wave, the wave is essentially linearly polarized (ignoring the higher frequency superposed oscillations). The interval begins at "B" and ends at "E". Thus, the nonlinear cyclotron wave has evolved into a wave led by a high frequency whistler packet followed by a nearly linearly polarized structure. The nonlinear "wave" contains both high frequency circular polarization plus low frequency linear polarization as well. We will say more about these features when discussing cometary waves.

Returning to Figure 5, one other noteworthy feature is the large angles of wave propagation relative to $\vec{B}$. Most cometary intervals analyzed have wave $\vec{k}$ directions at angles greater than 45°. This is even larger than waves in the Earth's foreshock, where typical values are - 10"-15° (Hoppe et al. 1981). These large angles have not been explained theoretically. Kojima et al. (1989), Kojima (1990) and Karamabadi et al. (1994) have been able to produce off-axis wave propagation at small angles (<30") by assuming a dominance of the ion perpendicular energy (within the distribution function) and also damping of parallel wave modes. However, even larger wave angles, typical of these waves at Jupiter, cannot easily be explained by the above mechanism.

The off-axis propagation feature of magnetosonic waves in foreshocks and at comets is crucial to much of what will be discussed here in this paper. This oblique propagation allows strong wave steepening, nonlinear wave deformation, and as we will see later, the start of possible "turbulent cascades". This is a point that we will return to later.

comets

An overview of the magnetic field associated with the solar wind interaction with comet Giacobini Zinner is shown in Figure 7. The coordinate system is GSE where $\hat{x}$ is towards the sun, $\hat{y}$ is in the $\hat{n} \times \hat{x}$ direction where $\hat{n}$ is in the north ecliptic pole direction, and $\hat{z}$ completes the right-hand system. The c1oscsl approach to the nucleus occurs at (-1100 UT). The bow wave/shock inbound and outbound crossings occur at -0930 UT and .-1215 UT and are at a - $\pm$ 105 km distance from the nucleus. The field has been displayed in polar angle coordinates so the "cometary turbulence" is readily apparent. Note that the fluctuations in δ (latitude angle) and ϕ (azimuth) arc large and arc not influenced by the bow shock/wave on either the inbound or outbound pass [there is some decrease in the fluctuations near the outbound pass, but this has been ascribed as being due to a directional change in the IMF near that time (Tsurutani and Smith, 1986). A change in this angle will result in a change in the pitch angle of the pickup ion beam and thus a change in growth rate of the resonant waves]. in this Figure, the waves found at distances up to $\pm 2 \times 10^5$ km from the nucleus are due to the free energy associated with heavy cometary ion pickup (H_2O^+, OH+, O+). To date, no major fraction of tile waves found at any of the comets explored (Grigg-Skjellerup [Glassmeier and Neubauer, 1993; Neubauer et al. 1993a], Halley [Glassmeier et al., 1989] and Giacobini-Z.inner [Tsurutani, 1991]) has been found to be associated with bow shock/wave reflected ions. It is possible that due to the presence of such strong turbulence generated by the pickup ion instabilities, such ions would be rapidly scattered before propagating very far from the shock. Another factor is that cometary bow shocks are quite weak (Smith et al, 1986; Neubauer, et al., 1986; 1993 b). Due to the solar wind mass loading, the shocks have Mach numbers of only -2.0 (Schmidt and Wegmann, 1991). Thus, particle reflection from such subcritical shocks would be expected to be quite weak or nonexistent.

The turbulence at comet GZ with measurable wave amplitudes extended to 7×10^5 km (Tsurutani et al., 1987). At Halley, where the bowshock was located at 1.1×10^6 km from the nucleus, the turbulence was detected at distances up to $3 \times$"106 km (Glassmeier et al, 1987) and for GS (which had the weakest neutral production rate and a bow shock location of 104 km), a distance of 2 x 104 km from the nucleus (Glassmeier and Neubauer, 1993).

Our paradigm of GZ wave development as a function of time (and also distance from GZ) is shown in schematic form in Figure 8. 'I'he figure illustrates the various wave features that were detected as the ICE spacecraft went through the turbulence from below to above. The solar wind comes from the left. The temporal evolution of the waves can be noted as ICE gets closer and closer to the comet nucleus. The reasoning is as follows: imagine a spherical shell of embyronic

9

sinusoidal waves first formed at -106 km from the nucleus. The idea is these embryonic waves would be sinusoidal and have small amplitudes when first formed. As the waves sunward of the comet get convected by the solar wind towards the nucleus, the continuous formation of cometary ions sunward of the comet gives additional free energy for continual amplitude growth. Thus the amplitudes will increase into the nonlinear range where phase-steepening (Cohen and Kulsrud, 1974; Tsurutani et al., 1987) will occur. This is illustrated in the next-to-botlom sketch. As the waves get driven harder or evolve further, they form whistler packets, shown in the third from the bottom pane]. The mechanism for this packet generation will be discussed later. Finally, very close to the bow shock, as the train of magnetosonic waves plus whistler packets expand further, they will run into their neighbor waves. At this point in time, some very interesting physical processes may occur. Wave-wave interactions such as the modulational or decay instabilities could lead to the creation of daughter or granddaughter waves, forming a fully turbulent plasma, However, we will show later that the waves around comet GZ and GS occupied too small of a spatial region to develop into a fully turbulent state (they quickly get convected into the downstream region). On the other hand, tbc comet Halley turbulence region was far larger (due to a much higher comet neutral gas production rate), and the measured 1 lalley turbulence dots not have well defined wave structures such as those at GS or GZ (Glassmeier et al., 1989). We are presently examining Halley to determine if such second or third generation waves are present or not.

The power spectra of the transverse magnetic field components of three comets are shown in Figure 9. The wave interval for each comet was selected just upstream of its bow shock/wave, so that the development of "turbulence" could be compared for similar scales. The power spectra of the two transverse components were averaged. From the Figure, first note that the power spectra at each comet is strongly peaked at -10-2 Hz, the water group ion cyclotron frequency. This is the "pump" wave for the cascade system. At frequencies higher than the pump, the power spectral fall-off has a $f^{-1.9}$ dependence for GZ, $f^{-2.1}$ for 1 lalley and $f^{-1.9}$ at GS. The power law spectra have suggested the possible development towards Kolmogorov or Kraichnan turbulence via wave-wave interactions (Tsurutani and Smith, 1986a; Acuna, 1987; Glassmeier et al., 1987). We will later show that this picture is perhaps too simplistic.

Figure 10 illustrates the GZ waves as they first begin to develop. This example is taken at a distance of 4.5×10^5 km from the nucleus. Waves at further distances are identifiable as cometary in nature, but have amplitudes too small for accurate minimum variance analyses. At this stage in their development, the wave magnitudes appear to have profiles similar to ocean waves: slow, gradual buildups in amplitude (from 0352:45 to 0353:45 and 0353:50 to 0355:10 UT) and abrupt

10

decreases at the "leading edges" which trail in time, (0353:50 and 0355:10 UT). It should be noted that the expected small amplitude sinusoidal waves were not observed at larger distances from the comet. All waves detected were somewhat steepened. 'I'his observation may be due to the large solar wind background fluctuations covering up the small amplitude waves, or that wave steepening proceeds quite rapidly, even at moderate wave amplitudes. At this time, the correct picture is not clear. Embryonic sinusoidal waves were not found at comet Halley as well.

The polarizations of the two wave "breakings" are shown in minimum variance coordinates in Figures 11 and 12. The leading portions correspond to planar waves with circular polarization. In both cases, the wave is left-hand polarized in the spacecraft frame, consistent with a right-hand wave that has been anomalously Doppler shifted to left-hand polarization by the solar wind convective flow. The waves are propagating at substantial angles relative to the ambient field, 29° and 40", respectively.

As waves develop further, wc have the situation shown in Figures 13 and 14. This example takes place at a distance of -2.5 x 10^5 km from the nucleus. This wave corresponds closely to the next to bottom schematic of Figure 8. In Figure 13, the trailing part of the magnetosonic wave (from 718:20 to 719:09, or from the beginning of the interval to point 1), is linearly polarized. This is indicated by the lack of phase rotation from points B to 1 in Figure 14, and is due to a purely compressive component of B_3 (and |B|) [see Figure 13]. Note that this polarization is not the typical transverse linear polarization that one ordinarily encounters. In this case, the polarization is due to a purely compressive component (wave-particle interaction will not result in pitch angle scattering, but particle mirroring).

Almost all of the 360" phase rotation of the wave occurs at the leading edge, between points 1 and 4 in the two Figures. In fact, there is -270'" of phase rotation from point 2 to 3, within 2 to 3s of the 100s wave. In terms of wave power, such as the power spectra shown in Figure 9, this represents some of the high frequency power in the "cascade" part of the spectrum. The wave is planar and left-hand circularly polarized in the spacecraft fi amt.

Figure 15, is a example of a wave at 1.6 x 10^5 km from the nucleus of GZ. The wave not only has developed into a nonlinear wave with a strong (Δ|B|/|B| - 1.0) compressive factor (from 6.5 nT to almost 13.0 nT), and a region of sharp phase rotation (- point 4), but some small amplitude upstream whistlers are present as wc]].

11

Even closer to the comet nucleus, we find a fully developed train of nonlinear waves plus their whistler packet precursors. This is shown in Figure 16. This event occurs at a distance of -10^5 km from the nucleus. Schematically, this corresponds to the third from the bottom panel of Figure 8. In the interval from 0915 to 0920, there are two magnetic magnitude peaks per -100s wave cycle, evidence of wave evolution that is not only detected in the wave data, but in simulations as well (Omidi and Winske, 1990). We will return to this topic shortly.

Figures 17 and 18 show a high frequency whistler packet in high resolution. The waves have -3s periods, arc left-hand circularly polarized in the plasma frame, and occur at the leading edge of a magnetosonic wave (not shown). The packet amplitude decreases linearly with distance from the magnetosonic wave, shown in the B_1 panel, This feature is similar to the Jovian foreshock wave illustrated earlier. The packet occurs in the spatial region near the upstream compressive ramp and serves to decrease the field magnitude from a peak value near -14 nT, down to an upstream field value of $\sim$10 nT. The B_1 - B_2 hodogram in Figure 18 shows this rotation (top panel). The other two holograms indicate that the packet is plane-polwizccl.

Figures 19 and 20 illustrate an example of further nonlinear development of magnetosonic waves. This example was taken at a distance of -1.6×10^5 km from the nucleus. At 0827 UT there is a decrease in |B|, leaving local peaks in B magnitude on either side. It appears as if the wave is splitting into two parts. Computer simulations have shown remarkably similar features (Figure 21, taken from Omidi and W inske, 1990). In the Omidi and Winske simulations they note that not only is wave-splitting occurring, but the leading half of the wave is traveling slightly faster than the average speed and the trailing portion slightly slower than the average, so the wave length is increasing with time. If these waves arc part of a multicycle wave train, then neighboring waves will eventually collide and perhaps interact, giving the 4th from bottom (and top) case of Figure 8. Intense wave-wave interactions may occur at this stage, with the start of the formation of a turbulent cascade.

A curious feature of this particular example is shown in Figure 20. In the region of wave splitting, from points 1 to 3 of Figure 19, there is a full 360" phase rotation of the magnetic field. The sense of rotation is right-hand polarized in the spacecraft frame. This can therefore be due to a right-hand wave in the plasma frame flowing in the downstream (solar wind) direction or a left-hand wave propagating in the sunward direction, but being anomalously Doppler-shifted by the solar wind convection flow. We cannot tell which of the two possibilities is the correct one. However if the former one is correct, this wave may be a daughter wave from a decay instability (Tsurutani et al., 1990). The wave has an -8s period.

12

From point 3 to the end of the interval, 0827:20 UT, there is a sharp wave phase rotation. It is left-hand circularly polarized in the spacecraft frame consistent with a right-hand polarized (whistler mode) wave in the plasma frame. The peak-to-peak amplitude is -13 nT in a 8 nT field magnitude.

Deep Foreshock Waves

A schematic of the waves in the Earth's foreshock was shown in Figure 3. What we wish to examine arc waves in the region of the foreshock where wave-wave collisions may have taken place. This cm-responds to the region on the far lower right of the Figure, the downstream region. The time that it takes to convect from the upper right part of the foreshock to the downstream region is longer than either the development time of waves detected at GZ or GS (in terms of ion cyclotron periods), and thus this is a good region of space to search for the presence of daughter and granddaughter waves. On the other hand, we should note that there is not a continual free energy source present, as for the cometary case. Thus, wave damping by cyclotron and Landau effects may overcome nonlinear effects and it is therefore. possible that such three-wave processes may not occur in the foreshock. This will be the first attempt to examine the Earth's foreshock for this possible phenomena. Figures 22 a,b,c show the IS} E-3 lunar encounters and the deep tail passes (Farquhar et al., 1986; Tsurutani et al., 1986). 'They also show 5 passes where ISEE-3 was in the foreshock of the Earth, but well downstream of the planet. It is these regions that are of prime interest to us here.

Onc example of turbulence-like magnetic field structure is given in Figure 23 in GSE coordinates. The fields are far more irregular than found in the upstream foreshock case (see examples in Hoppe et al., 1981). There arc no well-defined whistler packets or clearly periodic waves present.

The results of a coherency analysis is given in Figure 24. The coherence between B_1 and B_2 is typically 0.6 to 0.8 at frequencies between 3×10^{-2} to 5×10^{-2} Hz, and a phase lag of -90°. At frequencies from 10^{-1} Hz to 7×10^{-1} Hz, the coherency between B_1 and B_2 is 0.9 and the phase - –90". At the highest frequencies, >10 Hz, the coherency is -0.9 with zero phase lag. The first two intervals arc consistent with left-hand circularly polarized waves.

In this interval we have also found mixed polarizations. An example is shown in Figure 25. Within the interval 0113:29 to 0113:57 UT, there arc two ~360° phase rotations which seemingly have the opposite sense (top panel). Each wave has been analyzed separately (bottom two panels).

13

We find that they clearly have the opposite sense of polarity in the spacecraft frame. The one on the left has right-hand polarity and the one on the right, left-hand polarity. In each case, θ_{Bk}, the angle between the wave k vector and the x-axis (or the approximate solar wind flow direction), is small. Therefore there is little chance that this is due to a simple shift in the IMF orientation from a direction -parallel to -perpendicular (or vice versa) to V_{SW}. On the other hand, one cannot rule out the possibility that the two waves have the same plasma frame polarity, one propagating towards the sun and the other away. Further research is needed to resolve this problem.

From the time intervals given in Figure 25, the wave periods are - 10s and -7s respectivel y. Thus, the wave power would fall into the second frequency interval discussed previously. Therefore, the total amount of right-hand wave power present in the interval analyzed must be small or else the coherency anal yses would have indicated a linear polarizati on.

Interplanetary Discontinuities and Alfvén Waves

The plasma and field properties that can be used to distinguish four different types of discontinuities are listed in Table 1. The mass flux properties across the discontinuity surface, ρV_n, where p is density and V_n is the velocity normal to the discontinuity surface, are listed in column 2. The change in the tangential component of magnetic field 1 It, across the surface, and the normal component of the field, H_n, are listed in column 3. Of the 4 types of discontinuities potentially present in a hot plasma, contact discontinuities have not been reported in the solar wind, and are in many ways scientifically uninteresting. Shocks are present and have received considerable attention in the literature. However because shocks arc typically associated with high velocity stream structures, either impulsive coronal mass ejection events from the sun or steady high velocity flows from corona] holes, they are typically observed only once per week or so at 1 AU. Directional discontinuities, tangential and rotational, occur much more frequently, perhaps one or two per hour (Tsurutani and Smith, 1979; Lepping and Behannon, 1986).

An ideal tangential discontinuity has no mass flow and no field component normal to its surface. There can be a significant change in the tangential field component crossing the discontinuity surface, however. A rotational discontinuity can be thought of as a sharply kinked Alfvén wave. A rotational discontinuity dots have substantial mass flow across its surface, has a field component normal to its surface, and for isotropic plasmas, has a constant tangential field component magnitude.

14

A schematic illustrating these two types of discontinuities is illustrated in Figure 26. As can be seen, a tangential discontinuity can have totally different fields on either side of its surface. The magnitude and direction can be quite different. There is no field penetration of its surface, however. The total plasma plus magnetic pressure should be conserved across its boundary, $[B^2/4\pi + nkT] = O$.

The above descriptions are for idealized rotational and tangential discontinuities. Of course, real plasmas are not necessarily isotropic. And real discontinuities may have properties of both tangential and rotational discontinuities (Landau and Lifschitz, 1960). However even with these caveats, very few discontinuities have been found with ideal properties (within limits of the measurements). As an example, out of thousands of discontinuities examined, a (tangential) discontinuity with no normal component (at levels within the magnetometer sensor noise) has not been found. All have some significant normal component above measurement errors. The same is true for rotational discontinuities. Only a few have been found for which field magnitude is conserved (within measurement error).

Figure 27 is an example of a rotational discontinuity that almost fits the idealized model. The "thickness" is about 15s, corresponding to a scale of ~600 km. The rotation in minimum variance coordinates is shown in Figure 28. The normal component, B_3, is nonzero, but only slightly so. This is about as ideal an example as has been found by the authors and should be thought of as a relatively rare case.

A method of computerizing the selection of discontinuities using 1 min average IMF data was first devised by Tsurutani and Smith (1979). The criteria are A $\vec{B}$/111 $\geq$ 0.5 and $\Delta\vec{B} > 2\delta$ where δ is the variance on either side of the discontinuity. In a study using both Pioneer 10 and 11 magnetometer data when the two spacecraft were within 1 ° of radial alignment, the temporal variations were removed, leaving the radial dependence of discontinuity occurrence rates. The occurrence rates had fall-offs that varied exponentially with distance. It was concluded that this was due to a thickening of the discontinuity as a function of decreasing field strength. To normalize the rate to 1 AU, a factor $e^{(r-1)}/4$ was empirically derived, where r is in units of AU.

Figure 29 is the post-Jupiter Ulysses data as Ulysses goes from the equatorial plane to -50" latitude. The panels from the top are: the solar wind density, the magnetic field magnitude, the solar wind speed, the number of discontinuities day^{-1} calculated by the Tsurutani-Smith (TS) method, the number calculated by the Lepping-Behannon (1986) method and the satellite locations in distance and heliographic latitude. The important feature to note is that as Ulysses goes into and

out of the coronal hole high speed streams (increases and decreases in velocity, respectively), the number of discontinuities day^{-1} also increases and decreases in phase with the velocity variations. This discontinuity rate variability is not simply due to the increase in convection speed (shown in Tsurutani et al., 1995). As Ulysses reaches a high enough latitude so that it is permanently immersed in the polar coronal hole stream, the rate of discontinuity occurrence determined by the TS method is -150-200 day^{-1}, about 4 to 5 times that in the ecliptic plane at 1 AU. The primary cause of this relationship is shown in Figure 30. This is an interval at large (negative) heliospheric latitudes where the solar wind speed is a constant -700 km s^{-1}. The field components show a great deal of fluctuations due to the presence of Alfvén waves with $\Delta\vec{B}|/|B|$ -1 to 2. The waves are propagating outward from the sun (Tsurutani et al., 1994). The high Alfvénic fluctuation levels (at 1 AU) in high speed streams was first pointed out by Belcher and Davis (1971). Figure 31 shows the correlations between the SH components of $\vec{V}$ and $\vec{B}$. For this 24 h interval, all three components are correlated and have peak correlation coefficients at zero lag. This is consistent with the fluctuations being Alfvénic and the waves propagating radially outward.

Figure 32 is the magnetic field at 5.2 AU, at a latitude of -6.0°, in higher time resolution. Vertical lines indicate discontinuities detected by the TS method. From the Figure it can be noted that discontinuities often occur at the edges of the more slowly rotating Alfvén waves. We find that this relationship is readily apparent in 30-60 % of cases examined.

To determine the detailed relationship between discontinuities and Alfvén waves, we have performed minimum variance analyses on a dozen or so individual cases. Figure 33 illustrates the results of one case. In the top panel, the B_1-B_2 hodogram of the wave plus discontinuity interval is given. The time interval is 0508 to 0622 UT January 17, 1992. The field components were shown in Figure 32. In the hodogram, the field rotates from the far right, to the left and then back again. This comprises a ~360° rotation in phase.

We use the field minimum variance coordinate system determined from the analysis of the whole wave pulse discontinuity interval and plot the B_1-B_2 field relationships for the wave interval alone (left) and for the discontinuity interval alone (right). We find that the Alfvén wave rotates from the right to the left and then about halfway back, completing a rotation of ~270° in phase. The discontinuity is the other ~90° of phase rotation. It appears as though the discontinuity is the phase steepened edge of an Alfvén wave, very much like the cometary and foreshock wave steepened fronts. However, at this time, it is uncertain whether the Alfvén waves are steepened at their leading or trailing edges. This is because continuous Alfvén waves are present with sporadic discontinuities interspersed.

Because there is such a strong statistical relationship between Alfvén waves and discontinuities, it seems probable that many discontinuities (especially those in coronal hole high speed streams) are of a rotational nature, such as this one. If this assumption is correct, then these discontinuities do represent true wave power and simple power spectra (taken in high speed streams) may accurately give the inclusive wave power.

Conclusions

We have given selected examples illustrating the present status of LF nonlinear waves and turbulence. Nonlinear evolution of cometary, foreshock and interplanetary waves have demonstrated many fascinating examples, not all of which are theoretically well understood. Within these examples, we do not find obvious cases of fully developed turbulence, however. This probably indicates that the plasma has not had enough time for wave-wave interactions to dominate the spectra. The only space plasma case where this seems possible is at comet Halley, where the scale sizes are the largest yet encountered (see Tsurutani et al., 1995 for discussion) and perhaps in the downstream foreshock regions.

References

Belcher, J. and L. Davis, Jr., Large amplitude Alfvén waves in the interplanetary medium, 2, J. Geophys. Res., 76, 3534, 1971.

Brinca, A. L., Cometary linear instabilities: From profusion to perspective, in Cometary Plasma Processes. ed. by A. Johnstone, Am. Geophys. Un. Press, Wash, D. C., 61, 211, 1991.

Chen, F. F., Intro. Plasma Phys. Cont. Fus., Plenum Press, N. Y., 1, 1990.

Cohen, R. H. and R. M. Kulsrud, Nonlinear evolution of parallel propagating hydromagnetic waves, Phys. Fluids B. 17, 2215, 1975.

Farquhar, R, W., D. Muhonon and L. C. Church, Trajectories and orbital maneuvers for the ISEE-3/ICE comet mission, J. Astronaut. Sci. 1985.

Gary, S. P., Electromagnetic ion/ion instabilities and their consequences in space plasma: A review, Space Science Reviews 56, 373, 1991.

Glassmeier, K.-H., F. M. Neubauer, M. H. Acuna, and F. Mariani, Strong hydromagnetic fluctuations in the comet P/Halley magnetosphere, Astron. Astrophys. 187, 65, 1987.

Glassmeier, K.-11., A. J. Coates, M. H. Acuna, M. 1. Goldstein, A. D. Johnstone, F. M. Neubauer and H. Reme, Spectral characteristics of low frequency plasma turbulence upstream of comet P/Halley, J. Geophys. Res., 94, 37, 1989.

Glassmeier, K.-H. and F. M. Neubauer, Low frequency electromagnetic plasma waves at comet P/Grigg-Skjellerup: Overview anti spectral characteristics, J. Geophys. Res., 98, 20921, 1993.

Goldstein, M. L., C. W. Smith and W. H. Matthaeus, Large amplitude MHD waves upstream of the Jovian bow shock, J. Geophys. Res., 88, 9989, 1983.

Goldstein, M. L., H. K. Wong, A. F. Vinas, and C. H. Smith, Large amplitude MHD waves upstream of the Jovian bow shock: Reinterpretation, J. Geophys. Res., 90, 302, 1985.

Goldstein, M. L., H. K. Wong, and A. Eviatar, Excitation of MHD waves upstream of Jupiter by energetic sulfur or oxygen ions, J. Geophys. Res., 91, 7954, 1986.

Hoppe, M. M., C. T. Russell, L. A. Frank, T. E. Eastman and E. W. Greenstadt, Upstream hydromagnetic waves and their association with backstreaming ion populations: ISEE 1 and 2 observations, J. Geophys. Res., 86, 4471, 1981.

Karamabadi, H., D. Krauss-Varban, N. Omidi, S. A. Fuselier and M. Neugebauer, Low Frequency instabilities and the resulting velocity distributions of pickup ions at comet Halley, J. Geophys. Res., 99, 21541, 1994.

Kennel, C. F. and H. E. Petschek, Limit on stably trapped particle fluxes, J. Geophys. Res., 71, 1, 1966.

Kojima, H., H. Matsumoto, Y. Omura and B. T. Tsurutani, A study of wave instabilities driven by cometary ions, EOS, 70, 1182, 1989.

Kojima, H., A study of wave instabilities driven by cometary ions, masters thesis, Kyoto University, 1990.

Landau, L. D. and E. M. Lifschitz, Electrodynamics of Continuous Media, V.8 of Course of Theoretical Physics, Addison-Wesley, 224, 1960.

Lepping, R. P. and K. W. Behannon, Magnetic field directional discontinuities: Characteristics between 0.46 and 1.0 AU, J. Geophys. Res., 91, 8725, 1986.

Neubauer, F. M., K. H. Glassmeier, M. Pohl, J. Roederer, M. H. Acuna, L. F. Burlaga, N. F. Ness, G. Musmann, F. Mariani, M. K. Wallis, E. Ungstrup, and H. U. Schmidt, First results from the Giotto magnetometer at comet Halley, Nature, 321, 352, 1986.

Neubauer, F. M. K. H. Glassmeier, A. J. Coates, and A. D. Johnstone, lmw-frequency electromagnetic plasma wave fields at comet P/Grigg-Skjellerup. Analysis and interpretation, J. Geophys. Res., 98, 20937, 1993a.

Neubauer, F. M., et al., Preliminary results from the Giotto magnetometer experiment during the P/Grigg-Skjellerup encounter, Astron. Astrophys., 268.1.5, 1993b.

Omidi, N. and D. Winske, Steepening of kinetic magnetosonic waves into shocklets: Simulations and consequences for planetary shocks and comets, J. Geophys. Res., 95, 2281, 1990.

Roberts, D. A. and M. L. Goldstein, Res. Geophys. Supp., 932, 1991.

Schmidt, H. U. and R. Wegmann, An MHD model of cometary plasma and comparison with observations, in Cometary Plasma Processes, ed. A. D. Johnstone, Am. Geo. Univ. Press., 61, 49, 1991.

Smith, C. W., M.' L. Goldstein, and W. H. Matthaeus, Turbulence analysis of the Jovian upstream wave phenomenon, J. Geophys. Res., 88, 5581, 1983.

Smith, C. W., M. I.. Goldstein and W. H. Matthaeus, Corrections to Turbulence analysis of the Jovian upstream 'wave" phenomena, J. Geophys. Res., 89, 9159, 1984.

Smith, C. W, and M. A. Lee, Coupled hydromagnetic wave excitation and ion acceleration upstream of the Jovian bow shock, J. Geophys. Res., 91, 81, 1986.

Smith, E. J.. B. T. Tsurutani, J. A. Slavin, D. E. Jones, G. 1.. Siscoe and D. A. Mendis, International Cometary Explorer encounter with Giacobini-Zinner: Magnetic field observatory Science, 232, 382, 1986.

Smith E. J., and B. T. Tsurutani, Magnetosheath lion roars, J. Geophys. Res., 81, 2261, 1976.

Smith, E. J., B. T. Tsurutani, D. L. Chenette, T. F. Conlon and J. A. Simpson, Jovian electron bursts: Correlation with the interplanetary field direction and hydromagnetic waves, J. Geophys. Res., 81, 65, 1976.

Sonnerup, B.U. 0. and L. J. Cahill, Jr., Magnet opause structure and altitude from Explorer 12 observations, J. Geophys. Res., 72, 121, 1967.

Thorne, R. M. and B. T. Tsurutani, Resonant interactions between cometary ions and low-frequency electromagnetic waves, Planet. Space Sci. 35, 1501, 1987.

Tsurutani, B. T., Comets: A laboratory for plasma waves and instabilities in Cometary Plasma Processes, Geophys. Monogra. Ser., 61, ed. by A. Johnstone, Am. Geophys. Un. Press, Wash. D. C., 189, 1991.

Tsurutani, B. 'I'., B. E. Goldstein, M. E. Burton, D. E. Jones, A review of the ISEE-3 geotail magnetic field results, Planet. Space Sci., 34, 931, 1986.

Tsurutani, B. T., C. M. Ho, E. J. Smith, M. Neubauer, B., E. Goldstein, J. S. Mok, J. K. Arballo, A Balogh, D. J. Southwood and W. C. Feldman, The relationship between

interplanetary discontinuities and Alfvén waves: Ulysses observations. to appear in Geophys. Res. Lett., 1994.

Tsurutani B. T. and P. Rodriguez, Upstream waves and particles: An overview of ISEE results, J. Geophys. Res., 86, 4319, 1981.

Tsurutani, B. T. and E. J. Smith, Hydromagnetic waves and instabilities associated with cometary ion pickup: ICE observations, Geophys. Res. Lett., 13, 263, 1986.

Tsurutani, B. T., E. J. Smith, B. Buti, H. Matsumoto and A. Brinca, Discrete phase changes within nonlinear steepened magnetosonic waves: Comet Giacobini-Zinner, Geophys. Res. Lett., 17, 1817, 1990.

Tsurutani, B. T. and E. J. Smith, Interplanetary discontinuities: Temporal variations and the radial gradient from 1 to 8.5 AU, J. Geophys. Res., 84, 2773, 1979.

Tsurutani, B. T., R. M. Thorne, E. J. Smith, J. T. Gosling and H. Matsumoto, Steepened magnetosonic waves at comet Giacobini-Zinner, J. Geophys. Res., 92, 11074, 1987.

Tsurutani, B. T., D. J. Southwood, E. J. Smith and A. Balogh, A survey of low-frequency waves at Jupiter: The Ulysses encounter, J. Geophys. Res., 98, 21203, 1993.

Wu, C. S. and R. C. Davidson, Electromagnetic instabilities produced by neutral particle ionization in interplanetary space, J. Geophys. Res., 72, 5399, 1972.

Figure Captions

Figure 1. Two extreme cases of cometary ion interaction with the solar wind. In the top panel, the IMF is parallel to the solar wind flow. In this case, the ions will form a beam flowing at $-V_{SW}$ relative to the solar wind plasma. in the bottom panel, the IMF is orthogonal to the solar wind flow. The pickup ions will form a ring with velocity Vsw relative to the solar wind plasma.

Figure 2. Four different cyclotron resonant wave-particle interactions:two associated with ions and two with electrons.

Figure 3. A schematic showing the various waves and particles in a planetary foreshock.

Figure 4. An example of LF waves in the Jovian foreshock during a Pioneer flyby.

Figure 5. An example of LF waves in the Jovian foreshock during the Ulysses flyby.

Figure 6. Minimum variance analysis hodograms for the leading anti trailing portions of a LF wave shown in Figure 5.

Figure 7. The magnetic field turbulence near comet Giacobini-Zinner.

Figure 8. The expected nonlinear magnetosonic wave development along the ICE trajectory.

Figure 9. The power spectra of the transverse components of the magnetic fields for comets Giacobini-Zinner, Halley and Grigg-Skjellerup.

Figure 10. The G-Z waves at a distance of 4.5 $\times 10^5$ km from the nucleus. As a reference, the bow shock/wave was detected at a distance -105 km from the comet nucleus.

Figure 11. The hodograms for one of the waves in Figure 10. Minimum variance coordinates are used.

Figure 12. Same as for Figure 11.

Figure 13. An example of a G-Z wave that is both phase-steepened and highly compressive. This occurs at a distance of-2.5 x 10^5 km from the nucleus.

Figure 14. The hodogram for the wave event in Figure 13. Most ('-270") of the phase rotation occurs at the leading edge of the wave.

Figure 15. Further development of G-Z nonlinear waves as ICE approaches the comet nucleus. This event occurred at a distance of -1.6 x 105 km from the comet. The wave has a sharp phase rotation front plus small upstream whistlers. The magnetic magnitude compression is almost a factor of 2.

Figure 16. A fully developed train of nonlinear waves dctectcd at a distance -105 km from the comet nucleus. Whistler precursors are a common feature at this distance.

Figure 17. An example of a whistler precursor.

Figure 18. The hodograms for the Figure 17 event. The whistler packet is plane-polarized and its amplitude decreases linearly with increasing upstream distance from the magnetosonic wave.

Figure 19. A more complex magnetosonic wave that has appearances of splitting in half.

Figure 20. A B_1 - B_2 hodogram of the center portion of the interval of Figure 19. A wave with the opposite polarity, right-hand circularly polarized in the spacecraft frame, is present. This may be the product of a decay instability.

Figure 21. Wave splitting observed from computer simulation results (Omidi and Winske, 1990). This is similar to the G-Z results shown in Figure 19.

Figure 22. The ISEE-3 lunar cncounter/deep tail trajectories. ISEE-3 is sometimes in the foreshock region downstream of the Earth. Possible wave-wave interactions might be present in this region of space, where the wave temporal evolution has been considerably greater.

Figure 23. Turbulence-like magnetic fields detected within the Earth's downstream foreshock region.

Figure 24. A coherency analysis of the interval between the dashed vertical lines of Figure 23.

Figure 25. A right-hand circularly polarized wave immediately followed by a left-hand circularly polarized wave.

Figure 26. A schematic of an idealized tangential discontinuity (left-side) and a rotational discontinuity (ri,ght-side).

Figure 27. An example of an ideal rotational discontinuity (observed with the Pioneer 10 magnetometer). Such discontinuities with essentially no magnetic field magnitude change are relatively rare.

Figure 28. The B_1 - B_2 hodogram for the RD in Figure 27 and the B_3 component as a function of time.

Figure 29. The rate of occurrence of discontinuities as a function of solar wind streams (and heliographic latitude).

Figure 30. The relative constancy of discontinuity occurrence when Ulysses is within a polar coronal bole high speed stream. The rate of occurrence is about 4 to 5 times that in the ecliptic plane at 1AU.

Figure 31. The correlation between the interplanetary $\vec{V}_{SW}$ and $\vec{B}$ for day 251, 1993. The peak correlation coefficient occurrence at zero lag indicates that the fluctuations arc consistent with Alfvén waves propagating outward from the sun.

Figure 32. Interplanetary discontinuities (vertical lines) and Alfvén waves.

Figure 33. The phase relationship between the Alfvén wave and trailing (discontinuity.

Table Captions

Table 1. Jump conditions across four different types of discontinuities.

Reply to Referee No. 1

We thank the referee for his careful reading of the typescript and his helpful comments. We have addressed all of them in this revised version. We apologize for the previous lack of an abstract and figure captions. We were in a rush to make the deadline and forgot these important items.

page 2, line 3-5" corrected.

page 2, line 11: Corrected.

page 6: Deleted.

page 7: This has been revised to state that "off axis propagation leads to. . . . ."'

page 9: This has been corrected. In the sentence that you mention, we have changed the word "of" to "towards". We believe the spectra is in a state of evolution towards turbulence. But it is certainly not there. Thank you.

Reply to Referee 2.

We thank the referee for his helpful comments, We apologize for the haste in which the paper was written. The typos have been corrected and those areas which were unclear have been revised.

1. An abstract is now included.

2. Figure captions are now included. In Figure 9, each of the three panels corresponds to one comet. This is indicated in the panels.

WC have tried to better define the coordinate systems and the eigen values.

3. Corrected.

4. Corrected.

5. Corrected.

B_0 ⟶

V_{SW}

H_2O^+

$h\nu$

B_0

V_{SW}

H_2O^+

$h\nu$

Figure 1

$$\omega - \vec{k} \cdot \vec{v} = n\Omega$$

ions

u_R

R-mode

$v_\parallel$

u_L

I.-mode

$v_\parallel$

electrons

'L

L-mode

$v_\parallel$

u_R

R-mode

$v_\parallel$
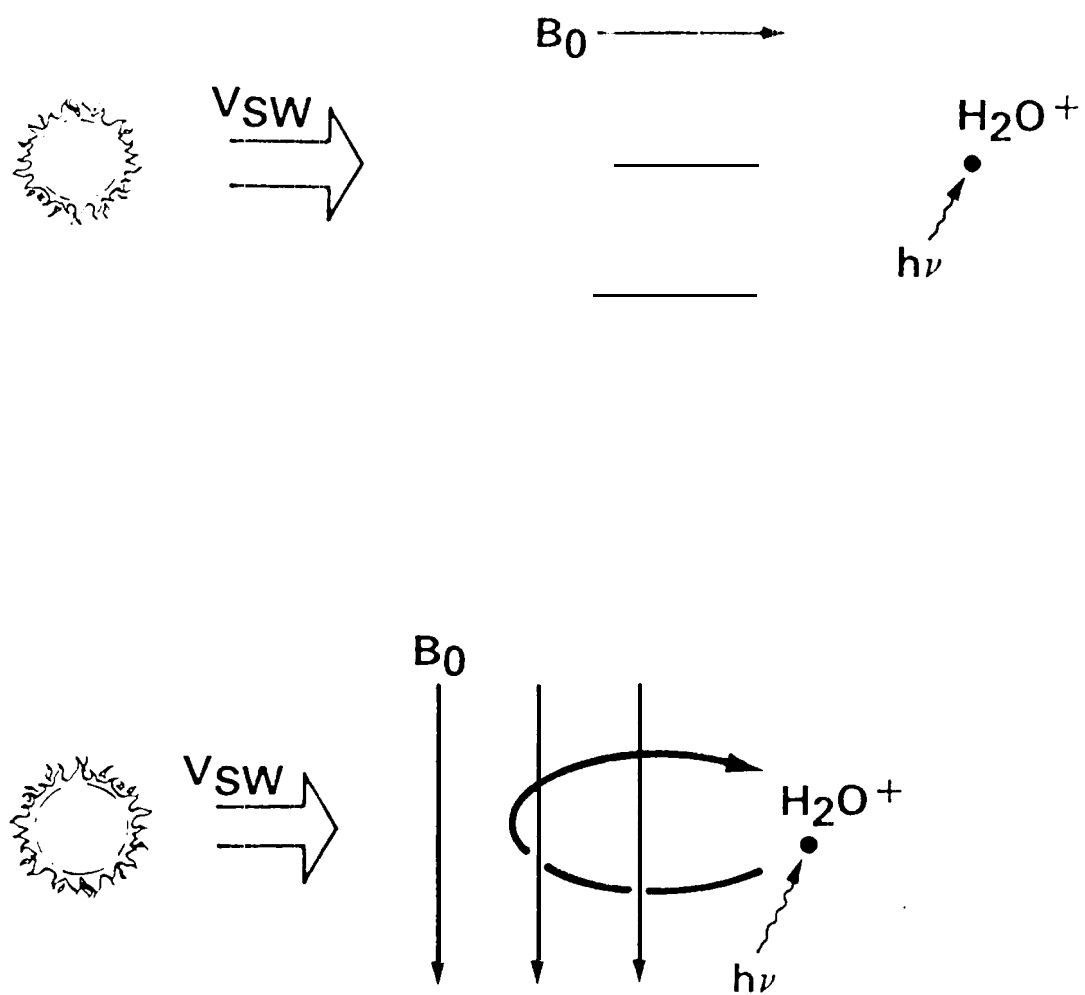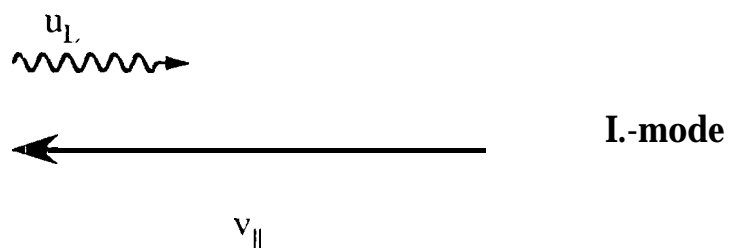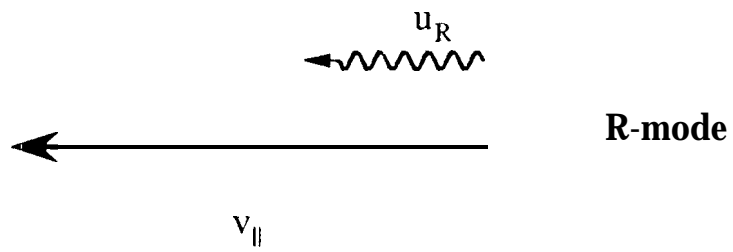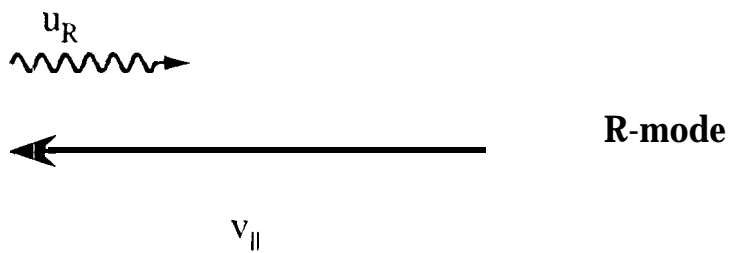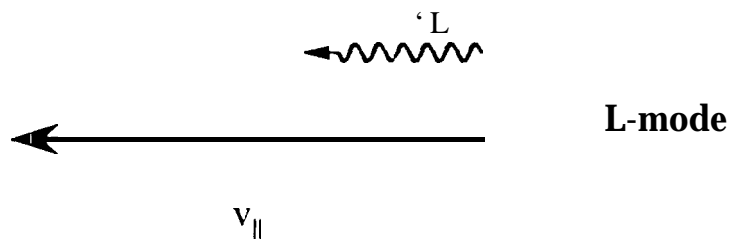
Figure 2

Figure 3

Figure 4
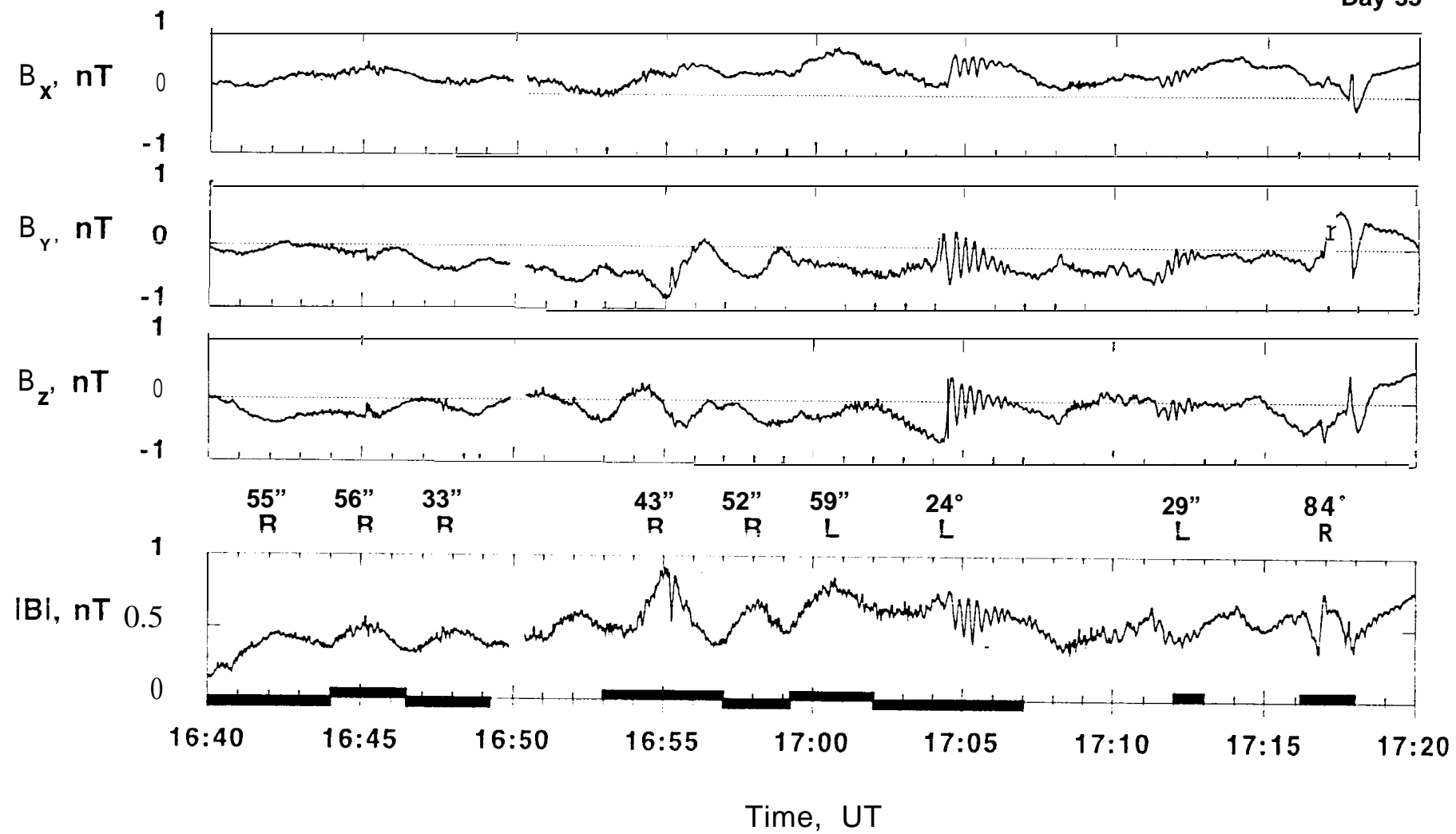
Figure 5

ULYSSES
February 2, 1992
Day 033

1702 - 1717 U.T.

$\theta_{BK} = 3\acute{o}$
$\lambda_1/\lambda_2 = 2.8$
$\lambda_2/\lambda_3 = 28$

B_1, nT

B_2, nT
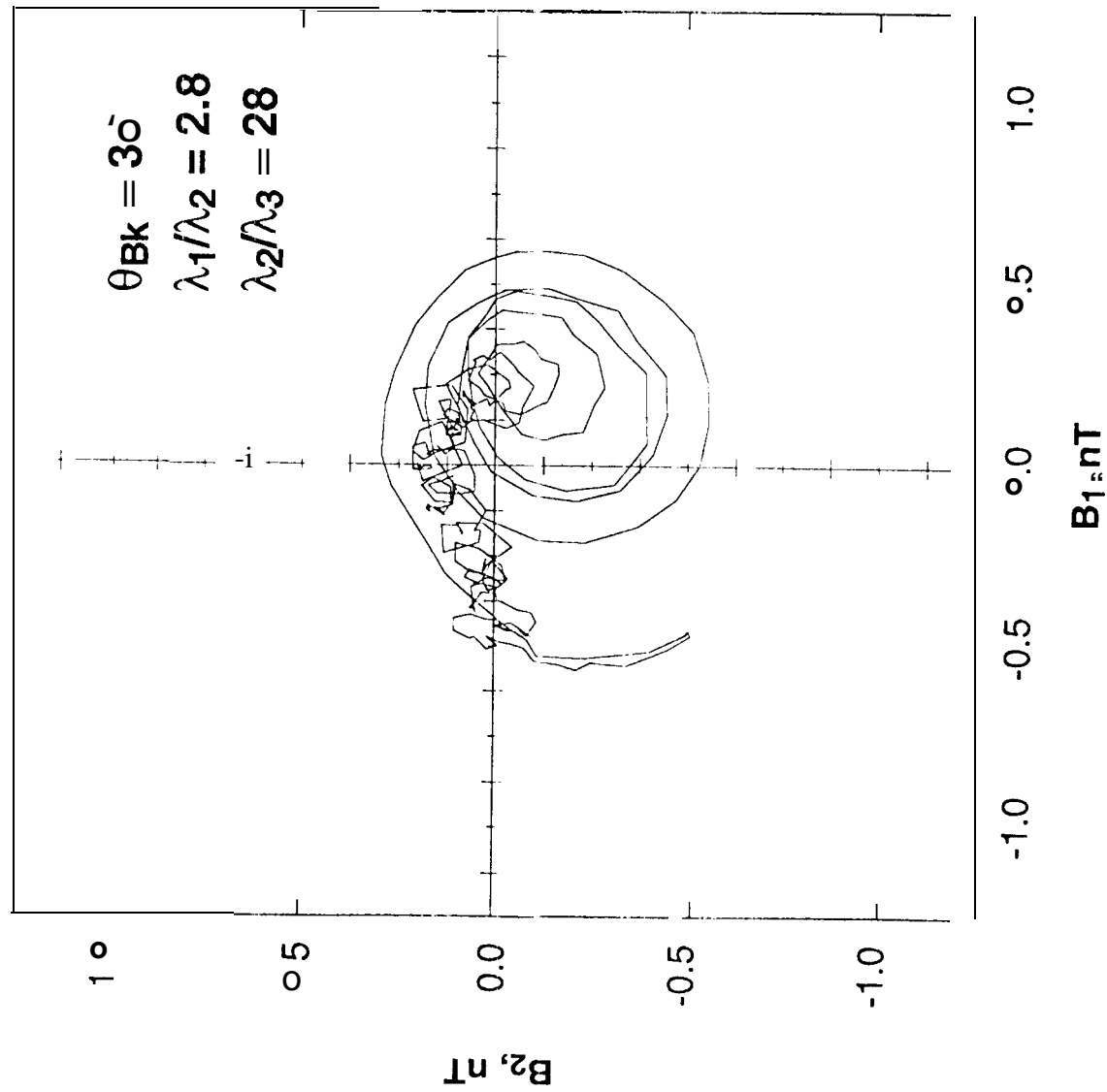
Figure 6a

ULYSSES
February 2, 1992
Day 033

1702:00-'1704:00 U.T.

$\theta_{Bk} = 12'$

$\lambda_1/\lambda_2 = 14.6$

$\lambda_2/\lambda_3 = 2.3$
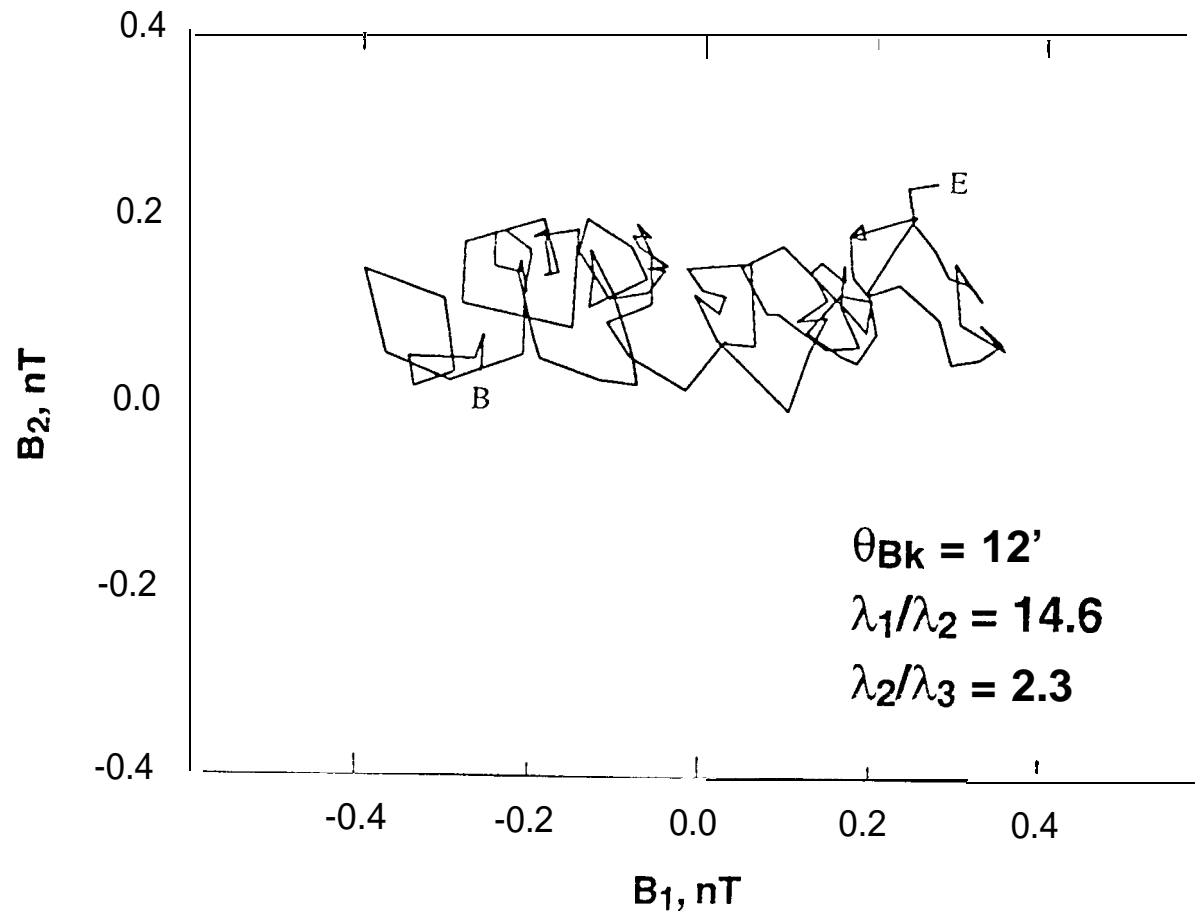
Figure 6b

SEPTEMBER 11, 1985
GSE COORDINATES
3 sec AVES.

Figure 7

ICE TRAJECTORY

BOW WAVE

GIACOBINI-ZINNER

10^5 km

106 km

Figure 8

Figure 9

ICE at Comet Giacobini-Zinner

September 11, 1985
Day 254
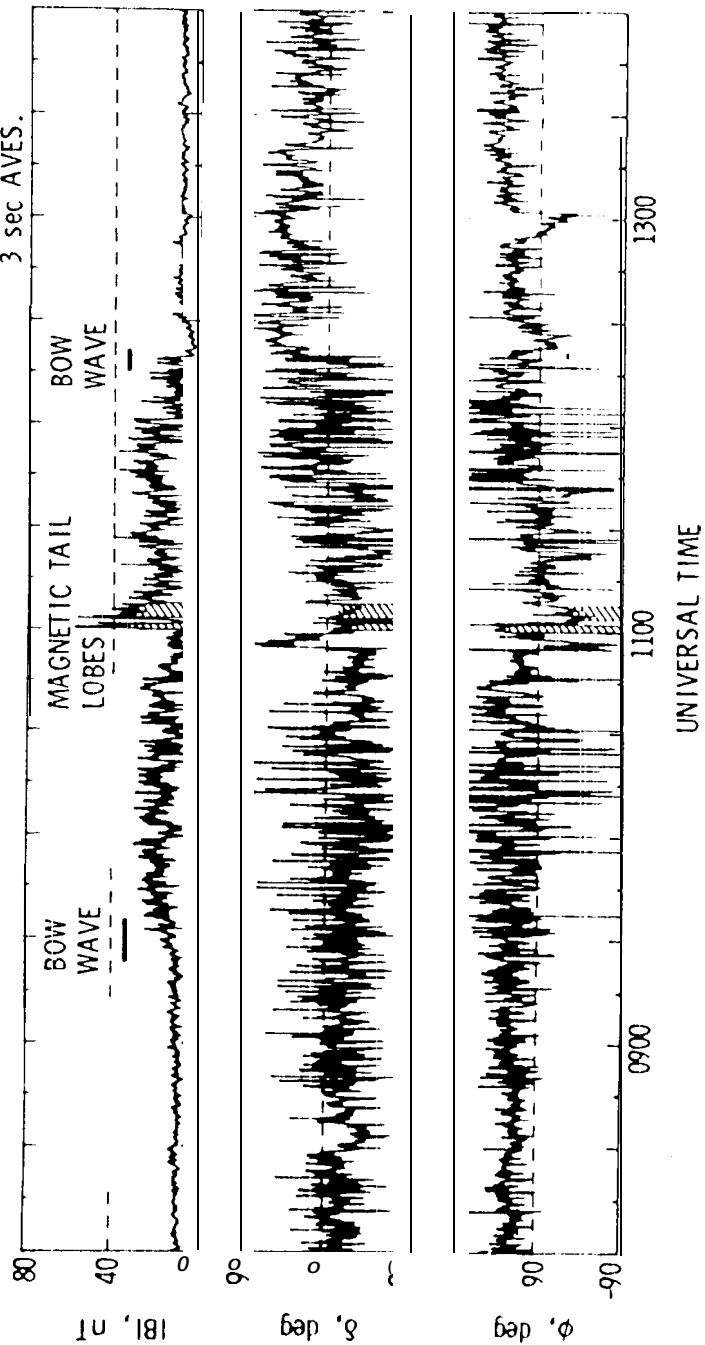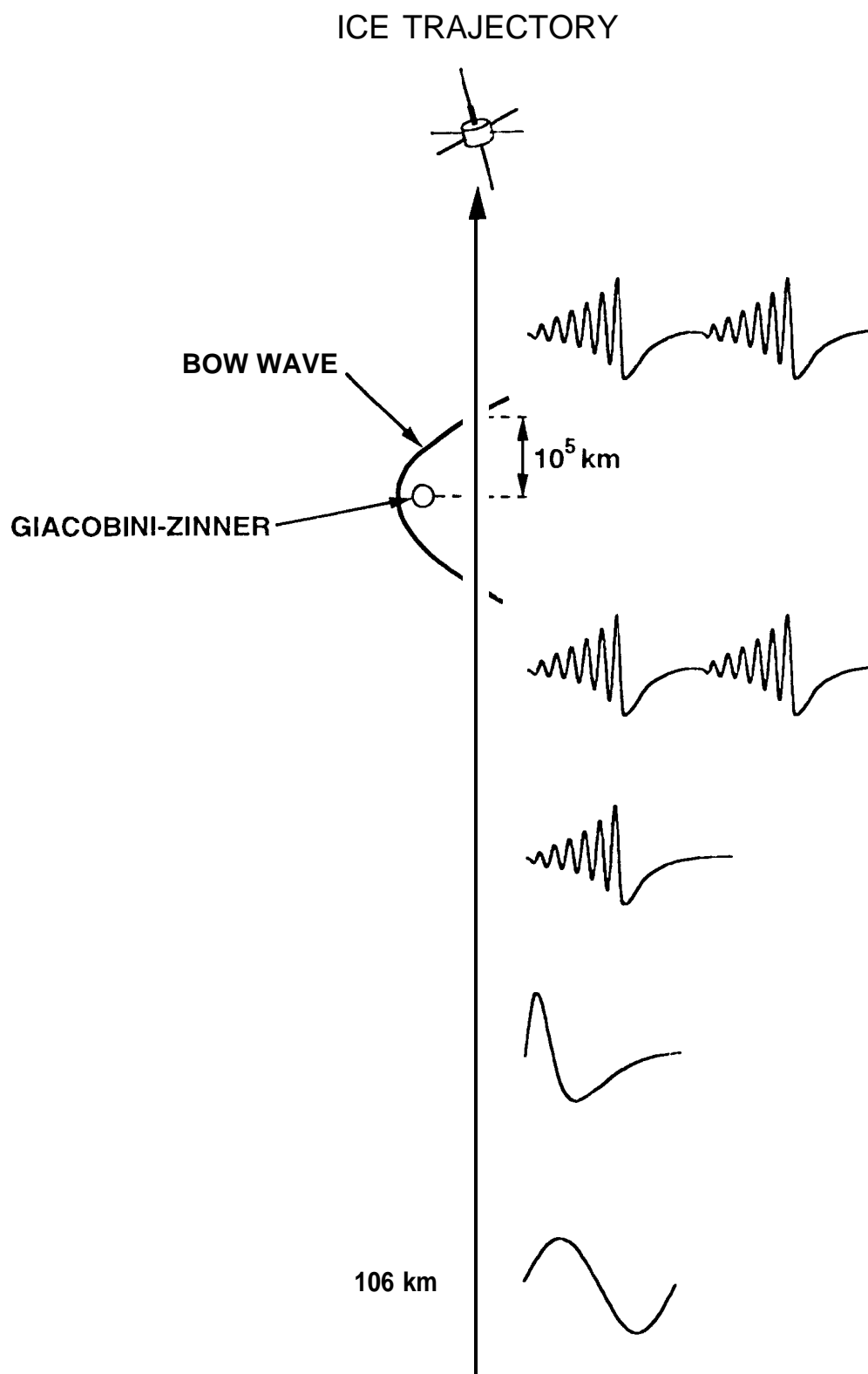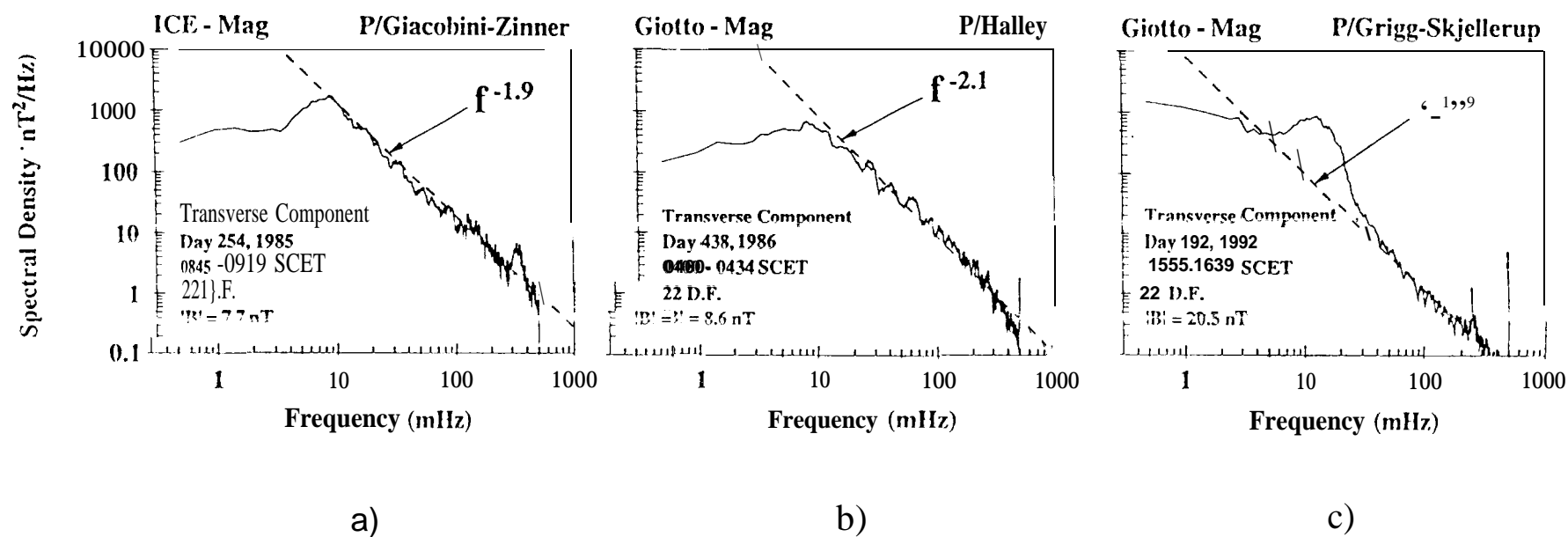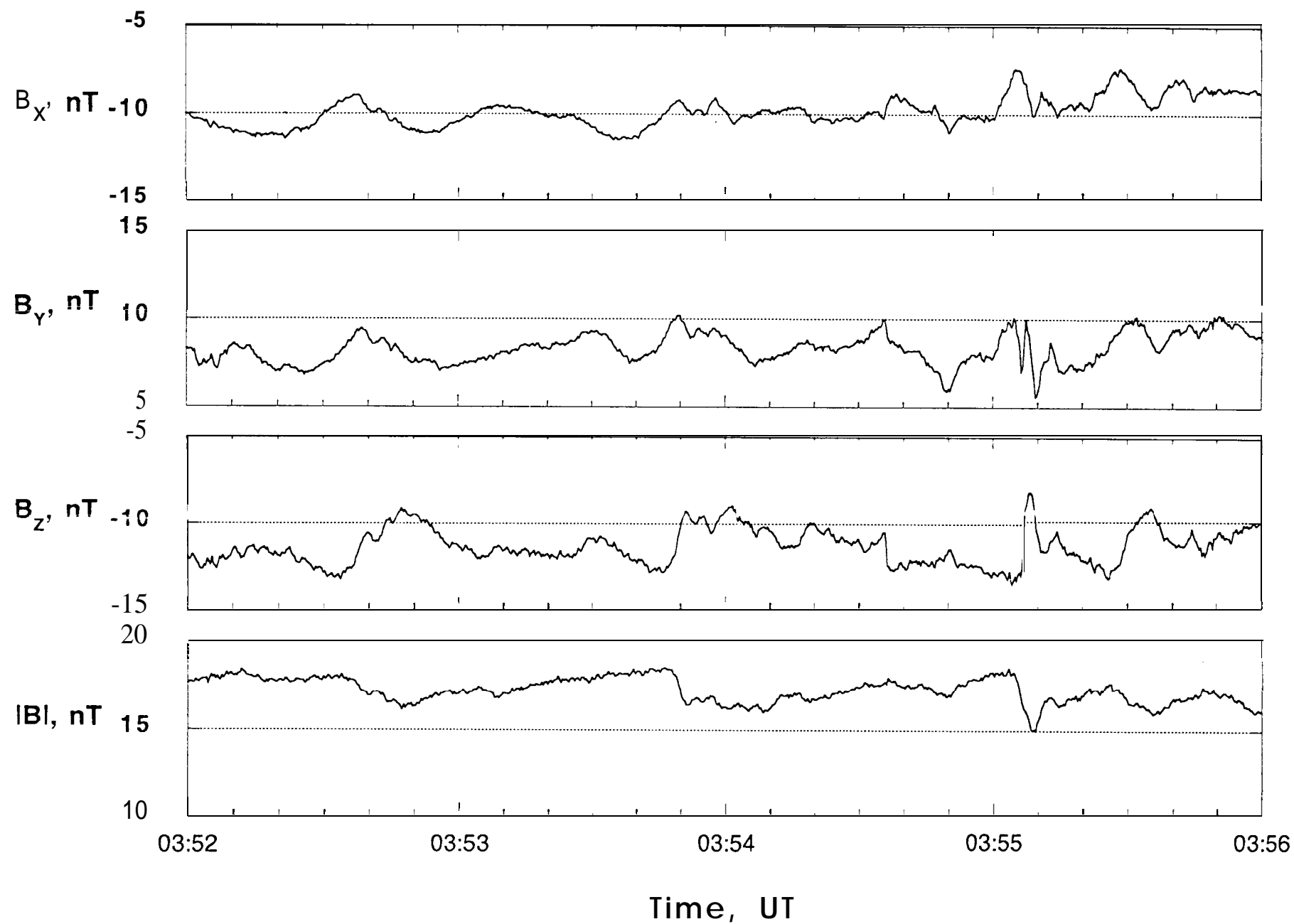
Figure 10

0352-0353 U.T.

$\lambda_1/\lambda_2 = 1.7$

$\lambda_2/\lambda_3 = 6.0$

$\theta_{kB} = 29^o$

L.H. POLARIZED

$\hat{B} \equiv -0.61, 0.45, -0.66$

B_2, nT

m .nT
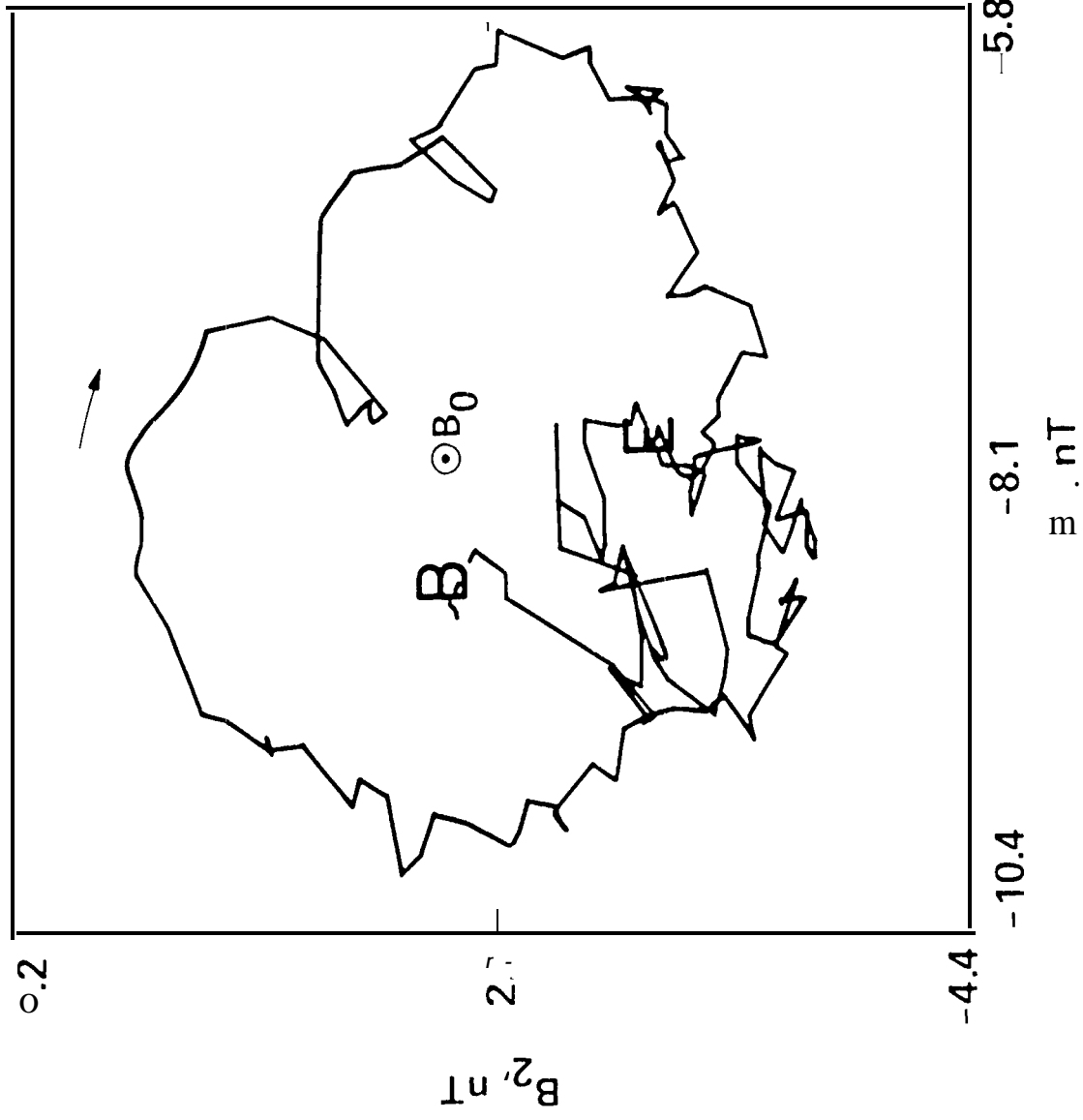
Figure 11

ICE
Day 254, 1985

0353:40-0353:55 U.T.

$\theta_{kB} = 40°$

L.H. Polarized

Multiple Rotation

$\hat{B} = (-0.57, 0.50, -0.65)$

$\lambda_1/\lambda_2 = 3.9$

$\lambda_2/\lambda_3 = 59$
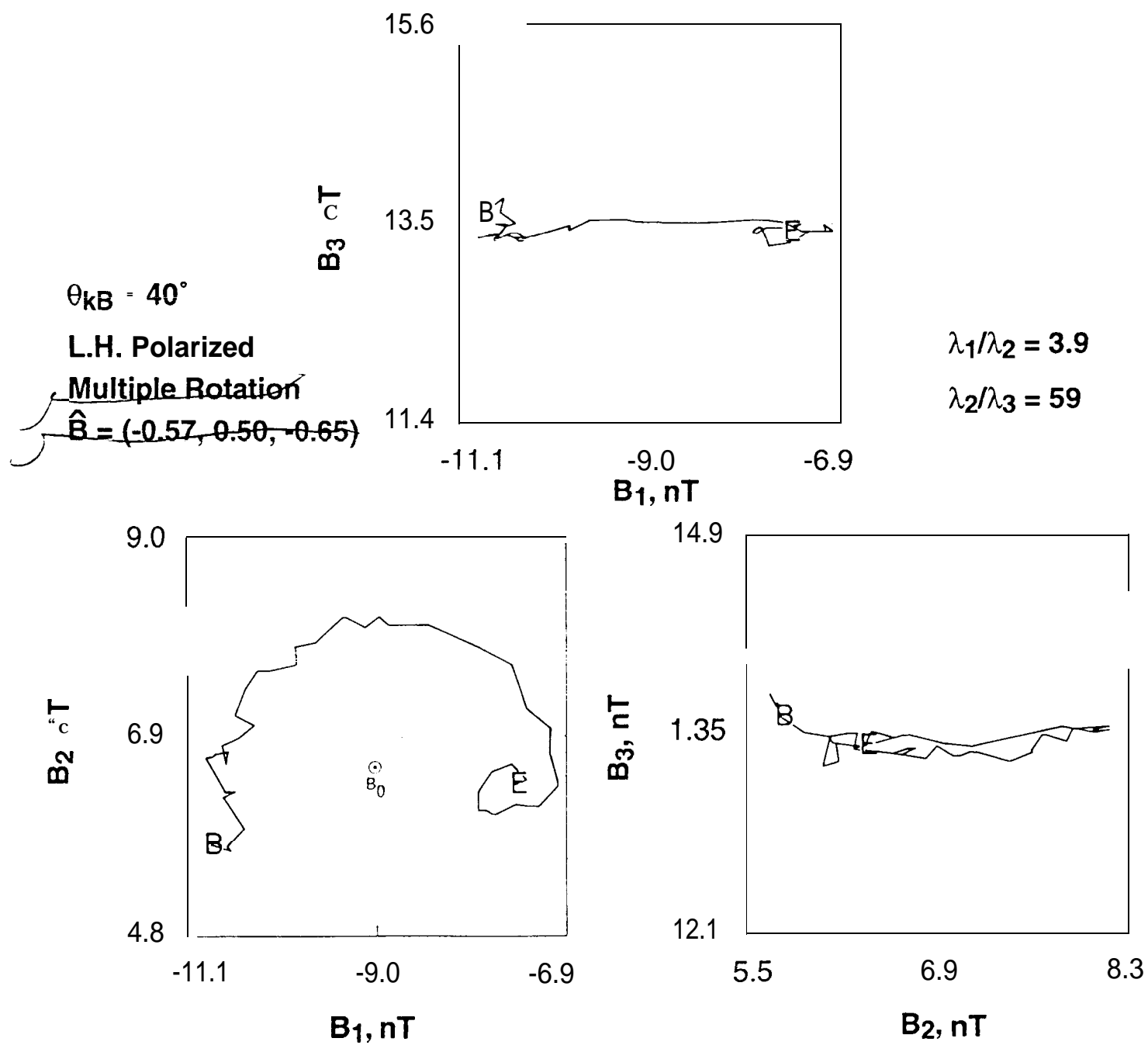
Figure 12

ICE   "
1985, Day 254
0718:20-0719:20   U.T.

θ_{kB} = 41 "
λ_1/λ_2 = 2.1
λ_2/λ_3 = 3.2
$\bar{n}$ = (-0.80, 0.57, -0.18)
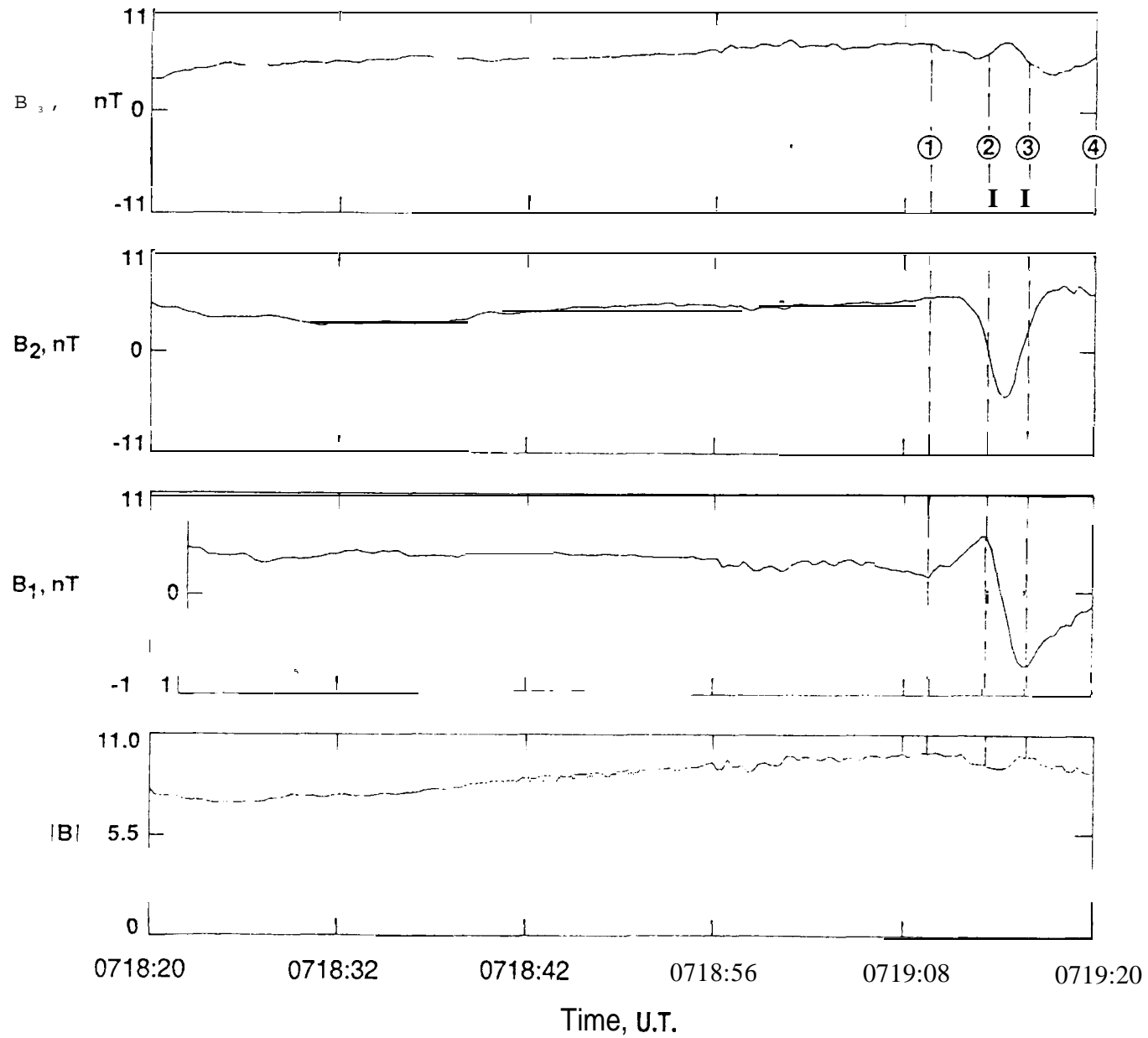
Figure 13

ICE
Day 254, 1985

0718:40 - 0719:21 U.T.
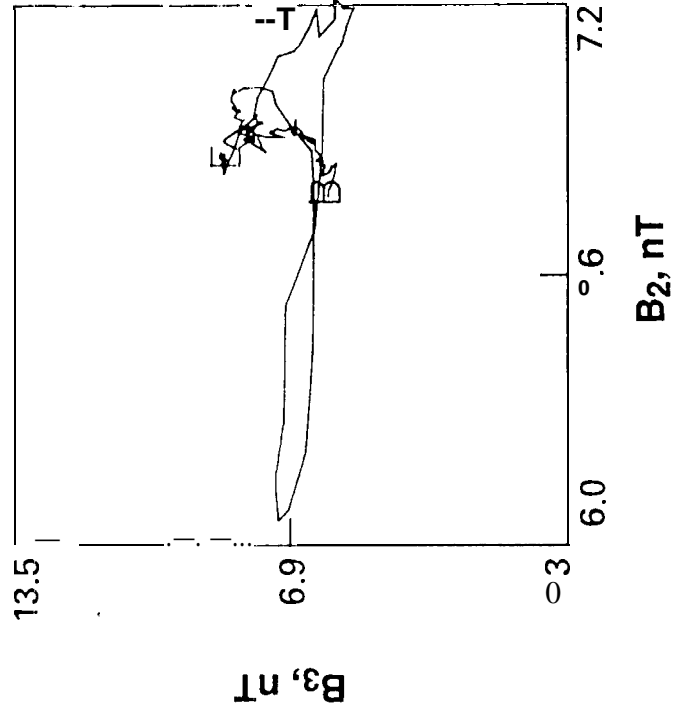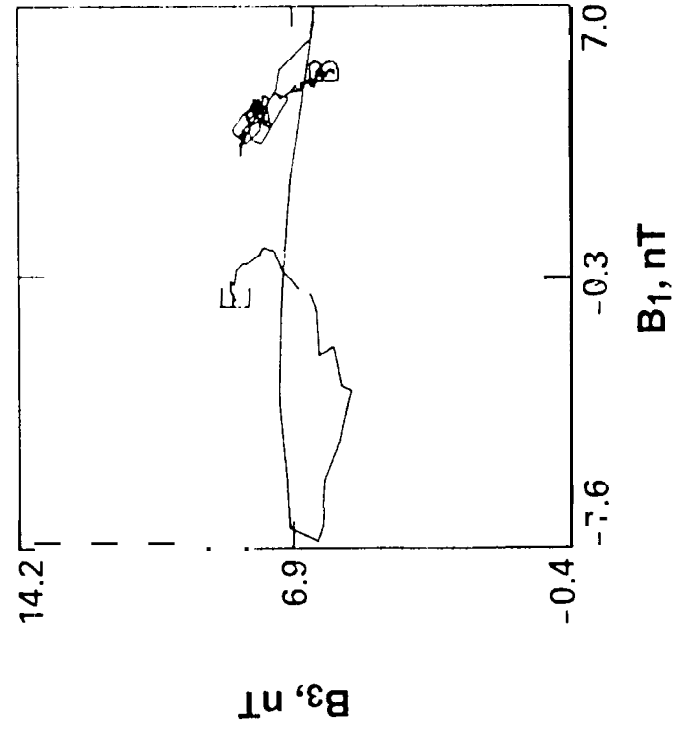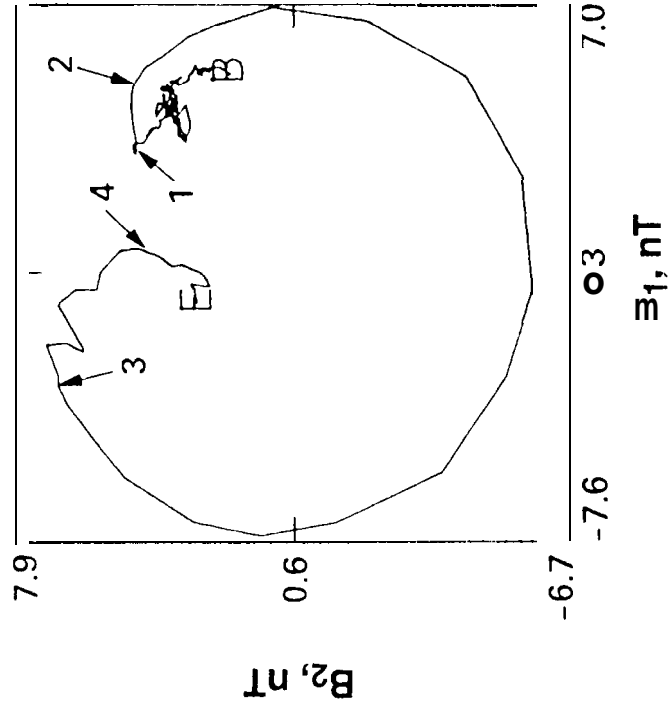
Figure 14

ICE
1985, Day 254
0823:38 - 0826:08 U.T.

$\theta_{kB} = 22°$
$\lambda_1/\lambda_2 = 1.5$
$\lambda_2/\lambda_3 = 6.6$
$\hat{n} = (-0.76, -0.61, 0.23)$
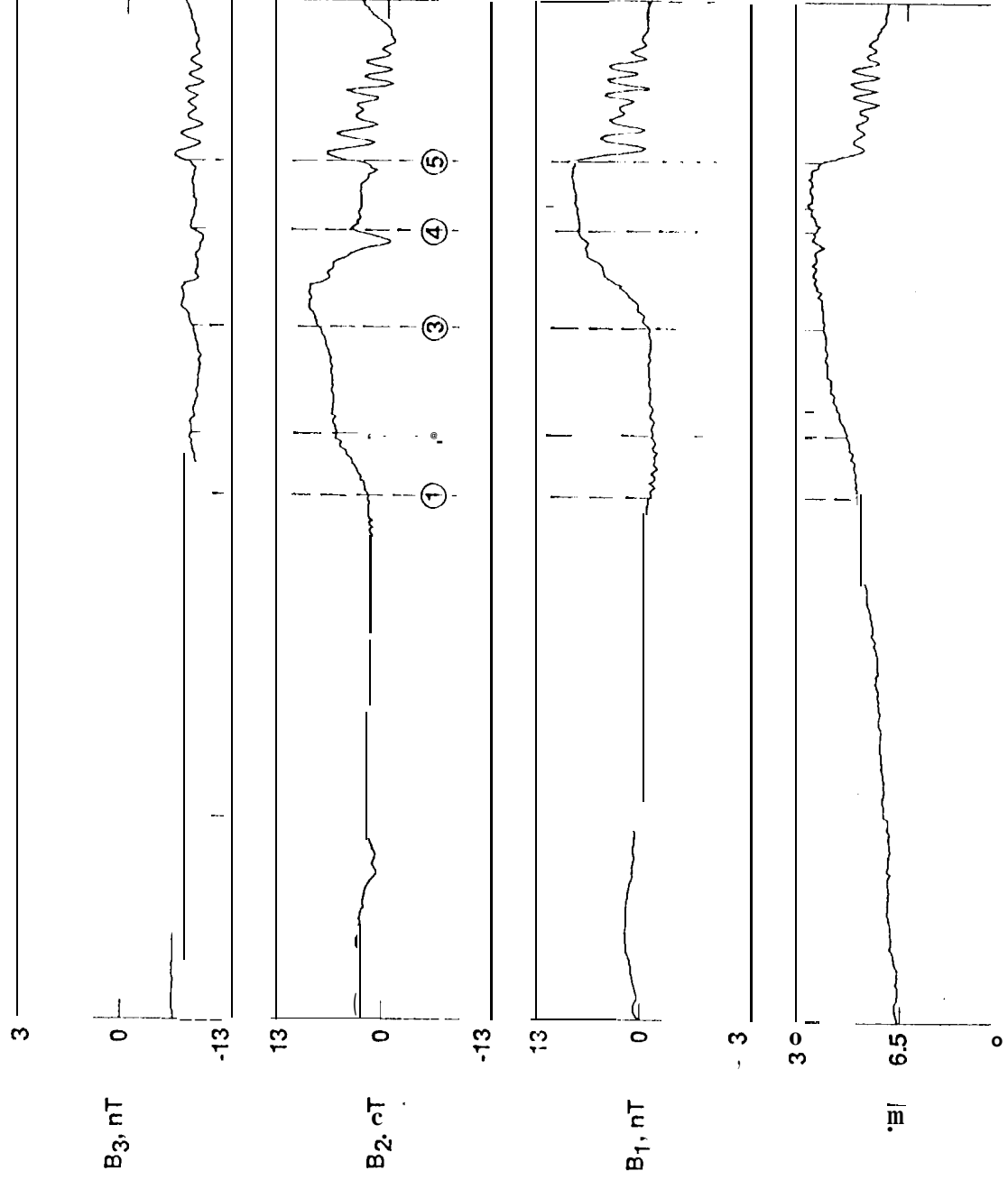
Figure 15

ICE at Comet Giacobini-Zinner

September 11, 1985
Day 254
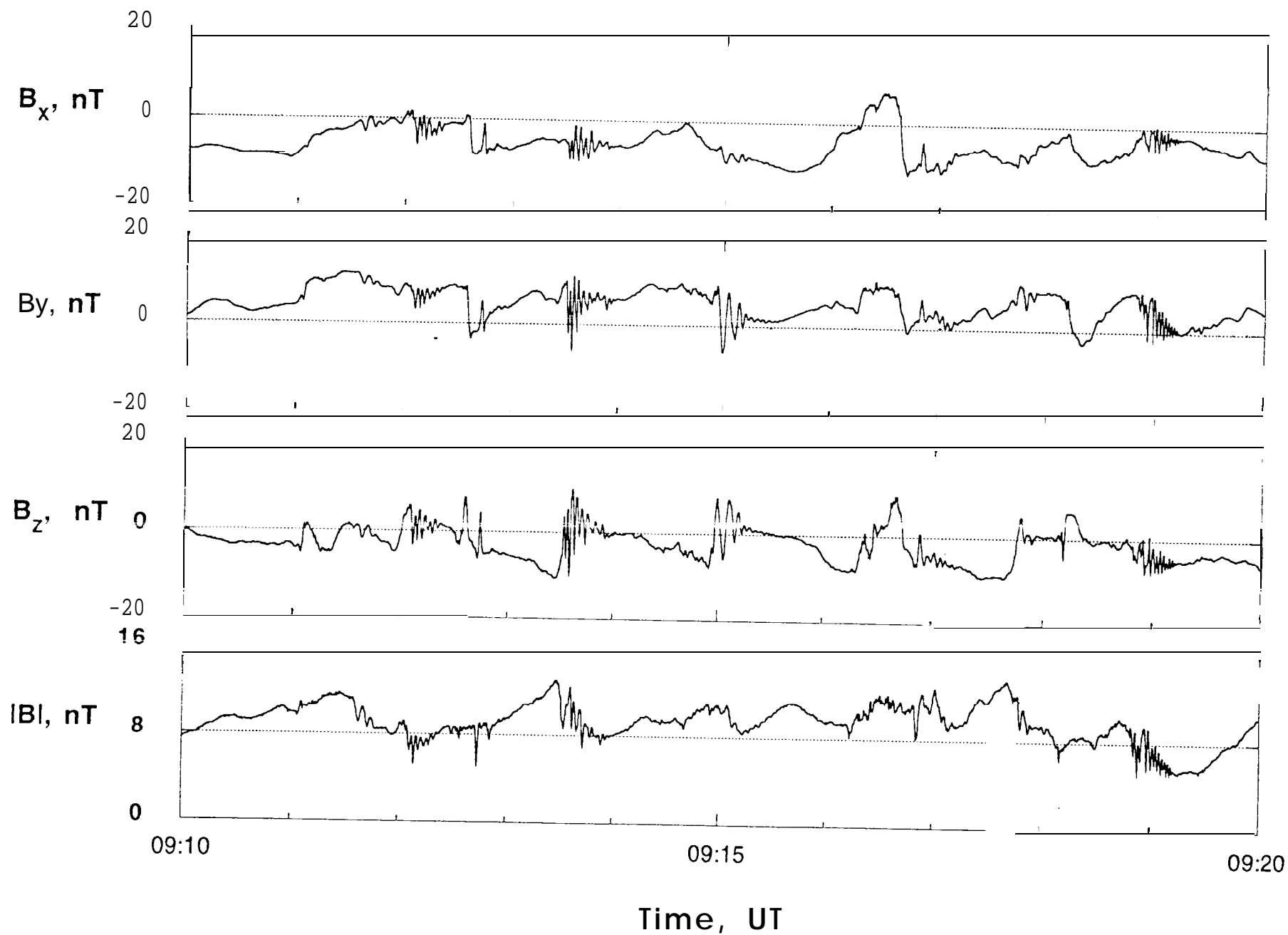
Figure 16
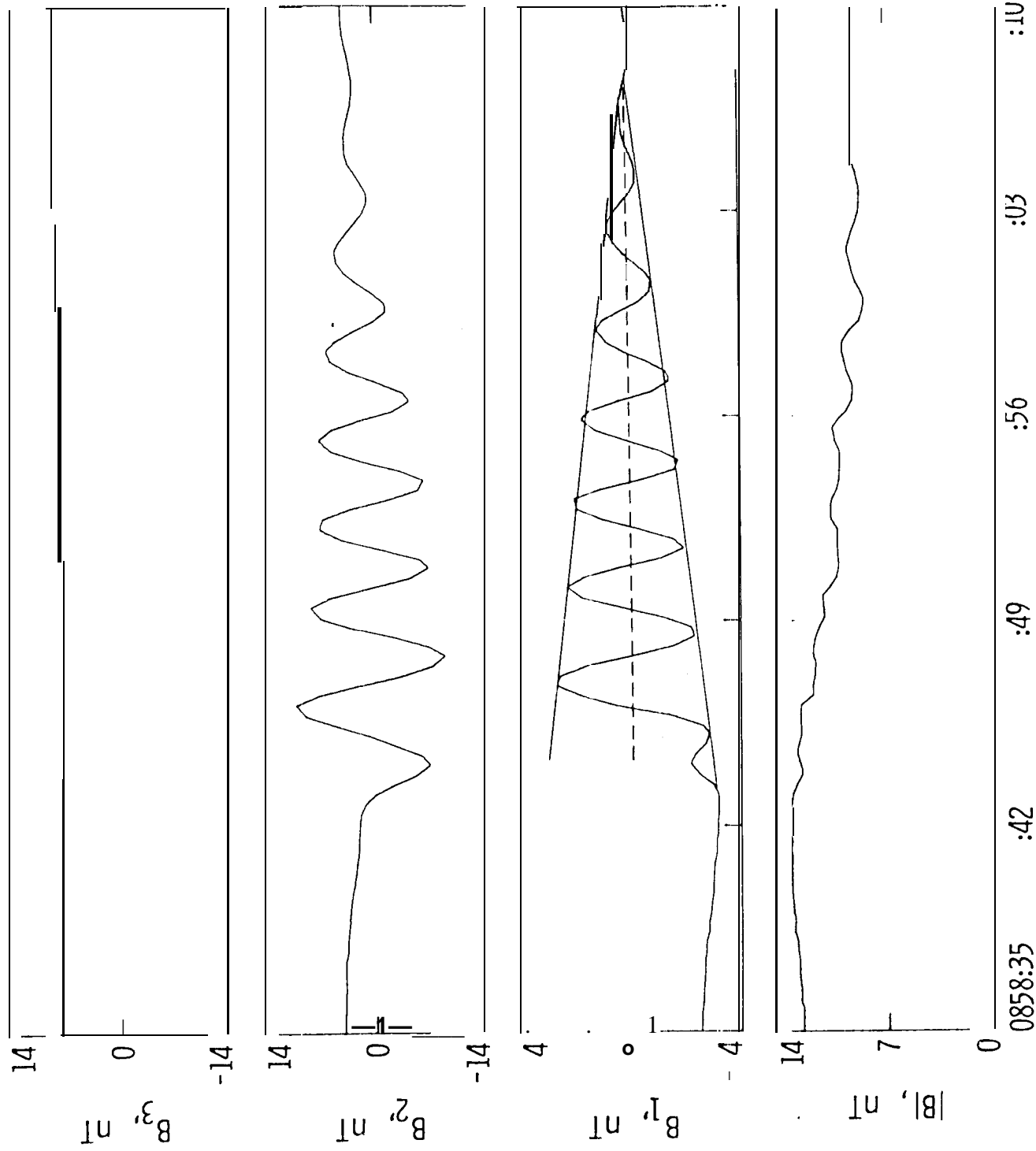
Figure 17

ICE
Day 254, 1985

0858:35 - 0859:1○U.T.
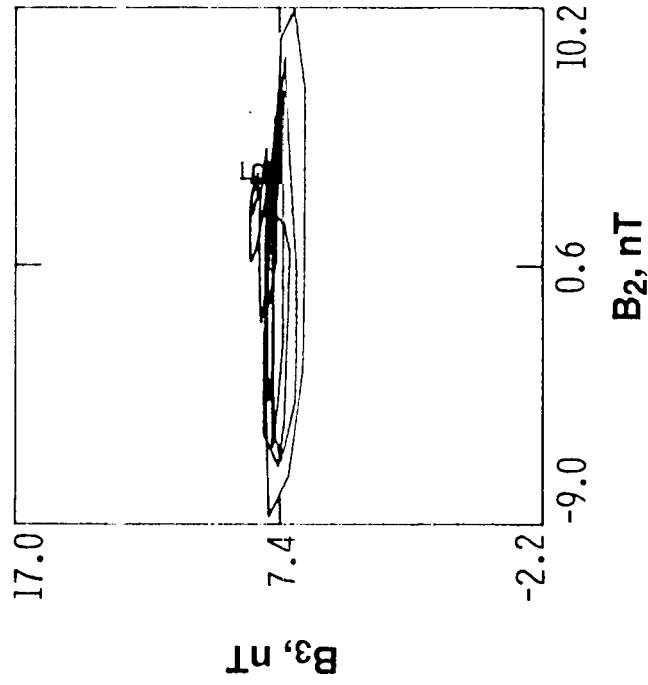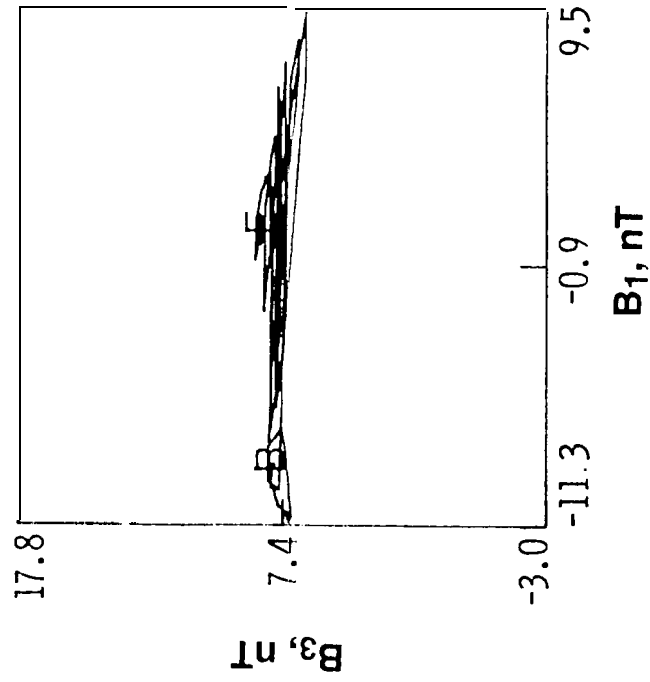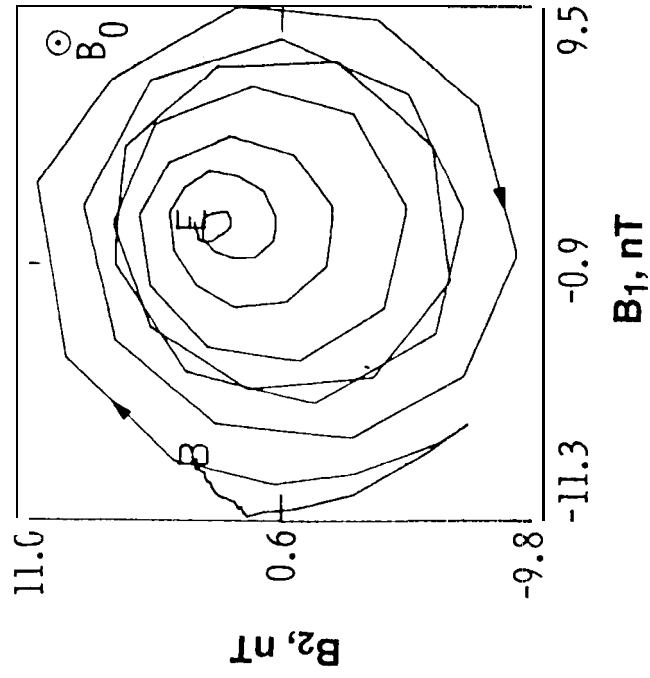
Figure 18

ICE
1985, Day **254**
0826:08-0827:44 U.T.

$\theta_{kB} = 3°$
$\lambda_1/\lambda_2 = 1.9$
$\lambda_2/\lambda_3 = 2.0$
$\hat{n} = (-0.84, 0.55, -0.04)$
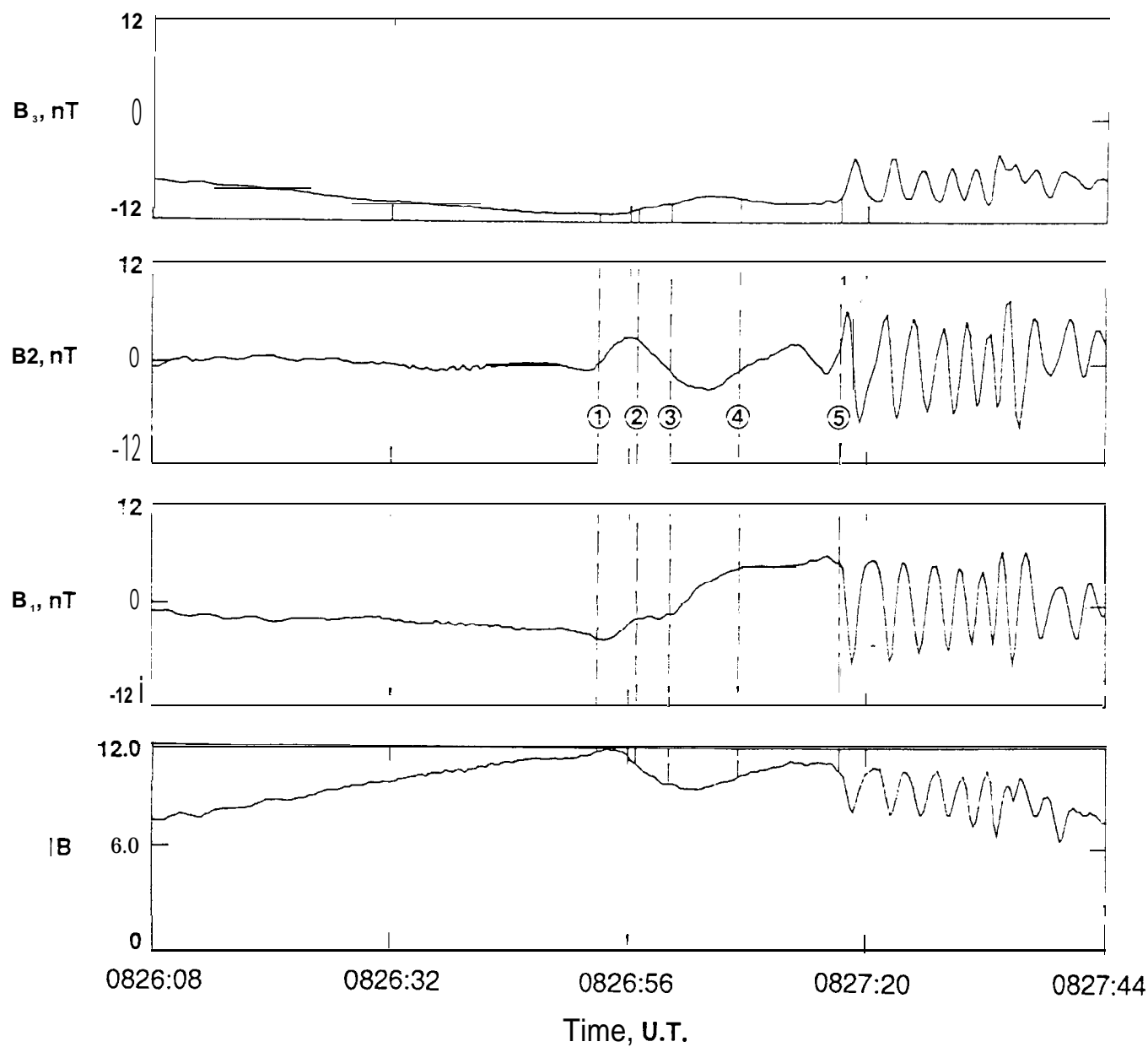
Figure 19

ICE
Day 254, 1985

0826:08-0827:2o

Figure 20

B

$\Omega_p t = 9.4$

$t \uparrow$

$\Omega_p t = 0.6$

0.0   37.5   75.0

$x \ (c/\omega_p)$
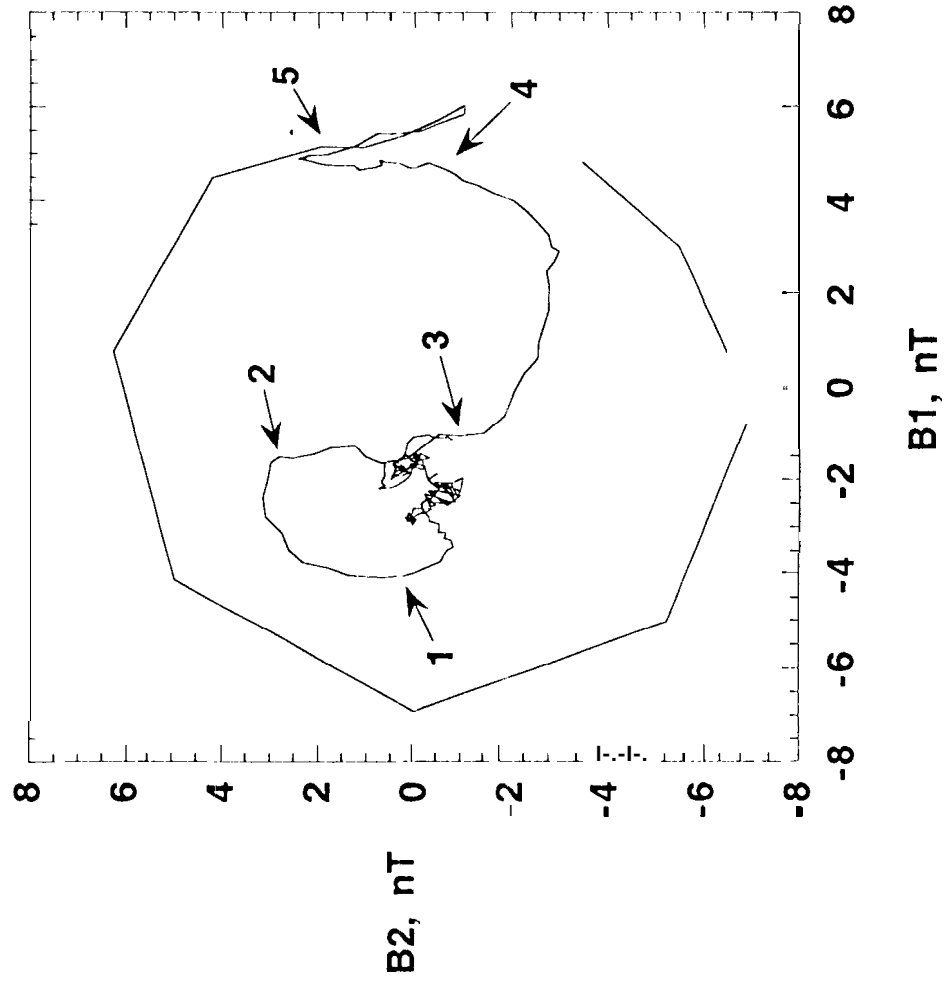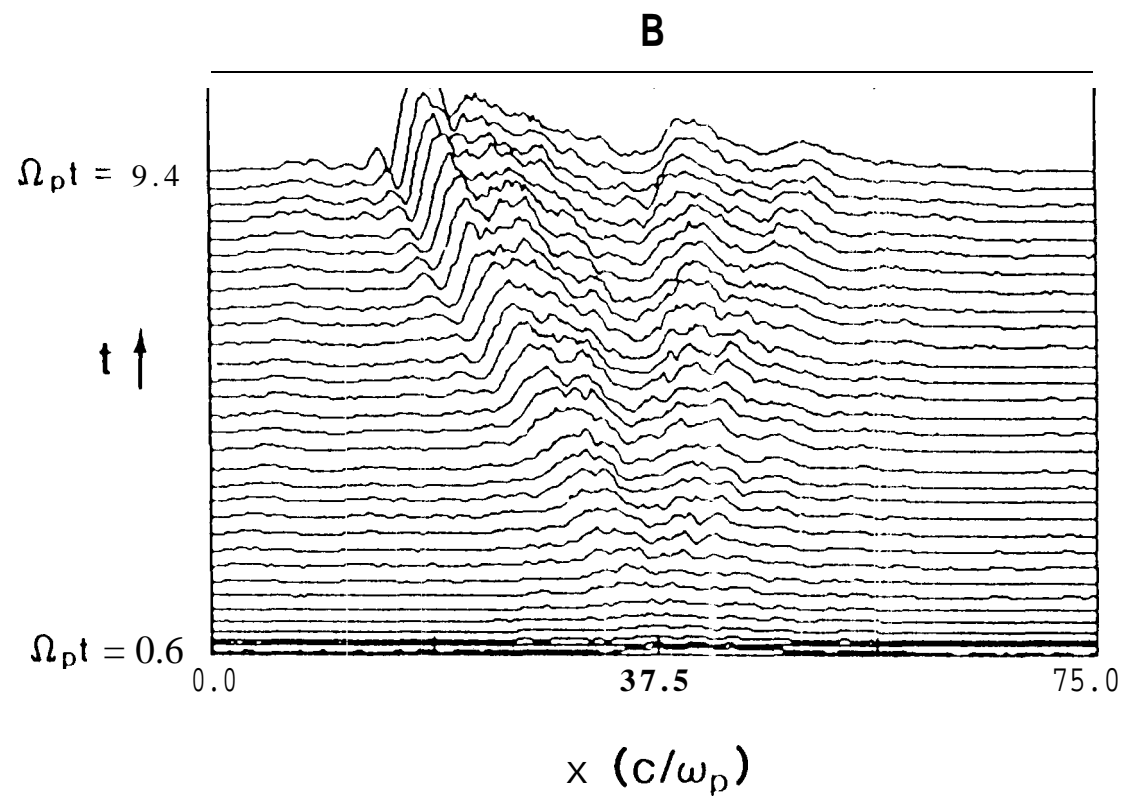
Figure21

ISEE -3 GEOTAIL PASSES 1 AND 2
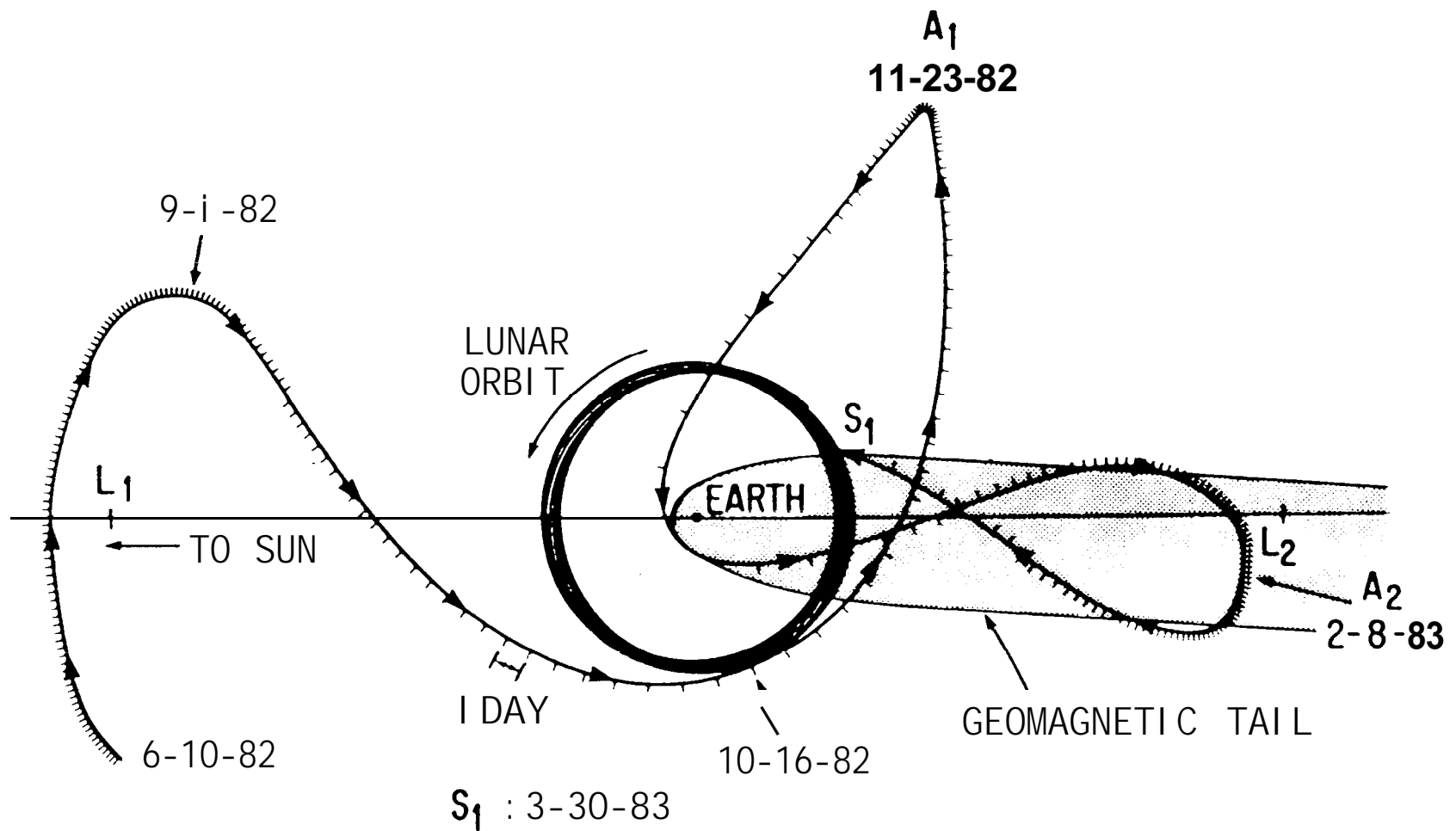
Figure 22a

ISEE-3 GEOTAIL PASSES 3 AND 4

1 DAY

LUNAR ORBIT

TO SUN

EARTH

S_1 : 3-30-83   LUNAR   Sw NGBY
A_3 : 4-11-83   APOGEE
S_2 : 4-23-83   LUNAR   Sw NGBY
A4 : 6-30-83   APOGEE
S3 : 9-27-83   LUNAR   SWINGBY
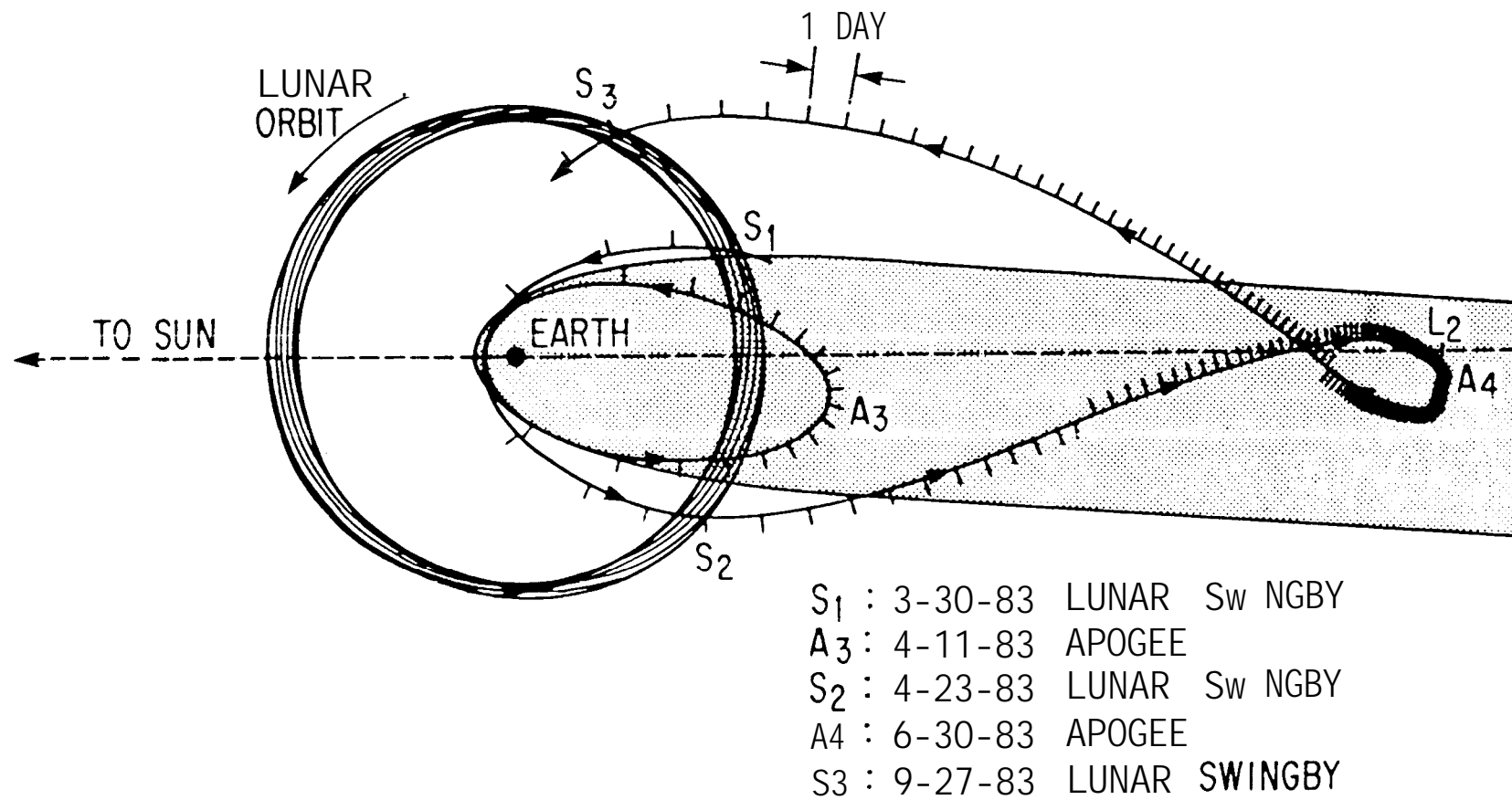
Figure 22b

ESCAPE TRAJECTORY

11-23-83

ISEE-3 Trajectory
Relative to Fixed
Sun-Earth Line

Escape Trajectory
$C_3 = 2.8 \ Km^2/Sec^2$

S3

1 Day

S5

To Sun

Earth

S4

Geomagnetic Tail

Lunar
Orbi t

S3: 9-27-83
S4: 10-21-83
S5: 12-22-83

Figure 22c

Figure 23

LOG POWER(nT^2/Hz) vs LOG FREQUENCY(HZ)
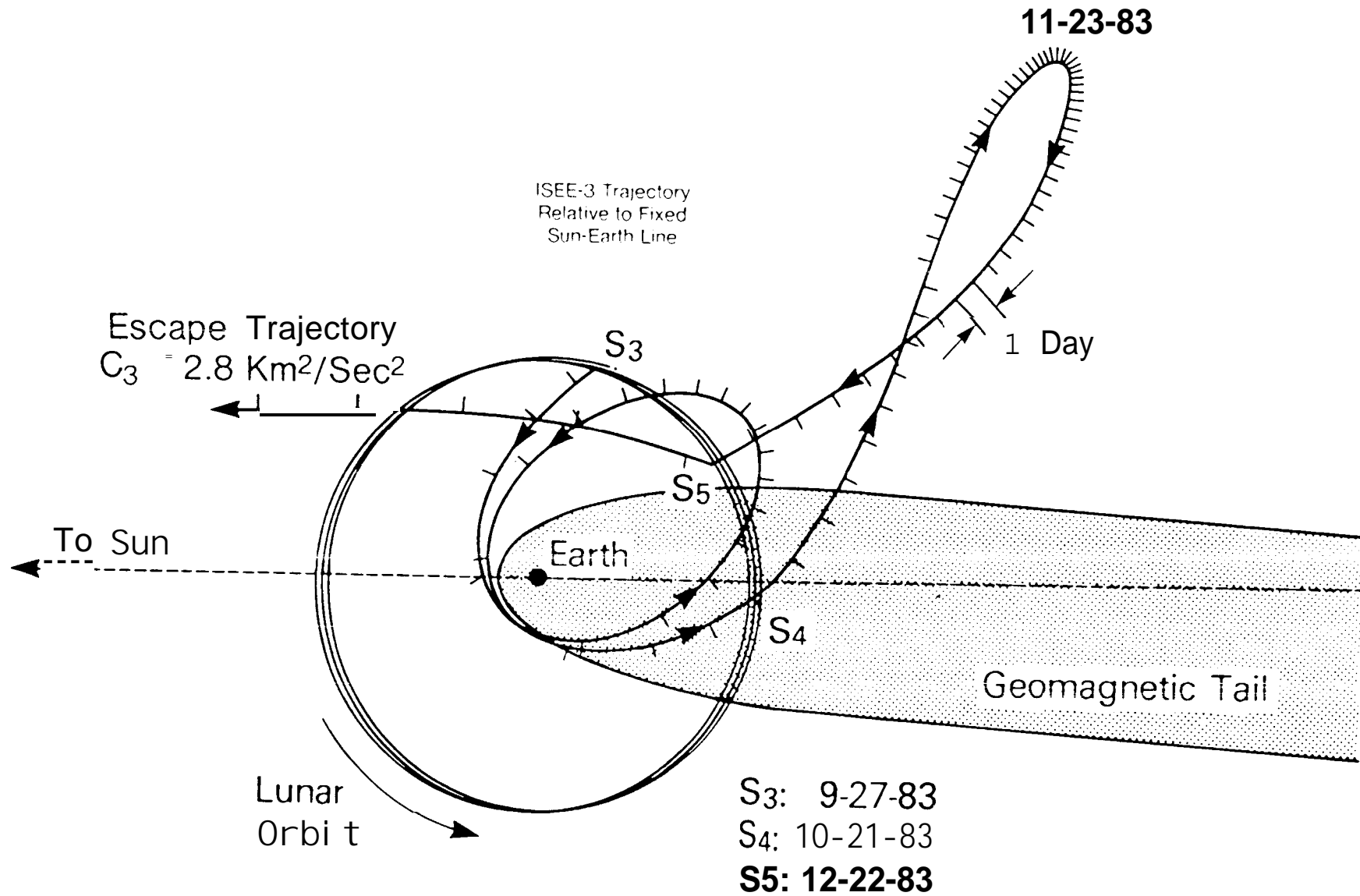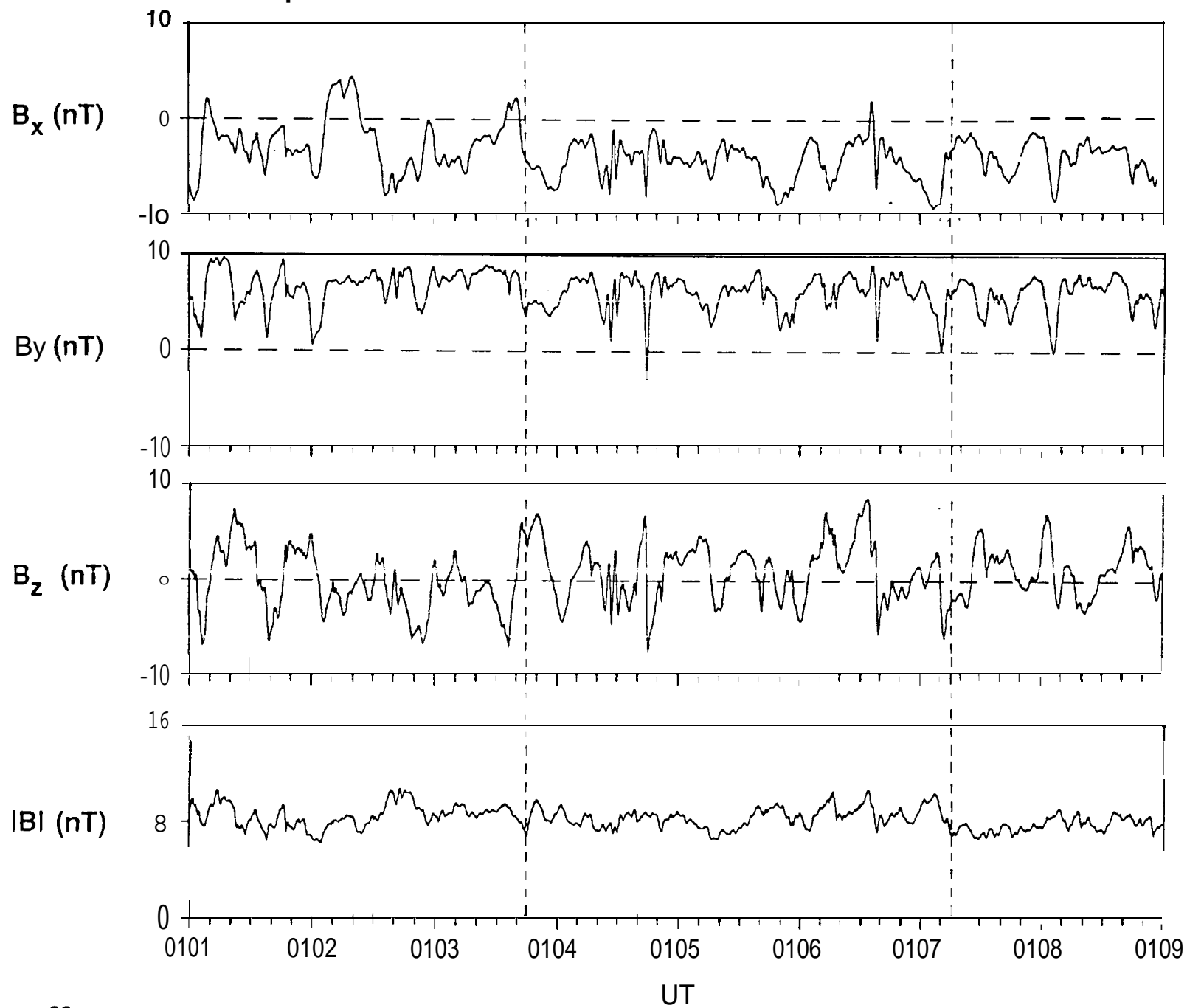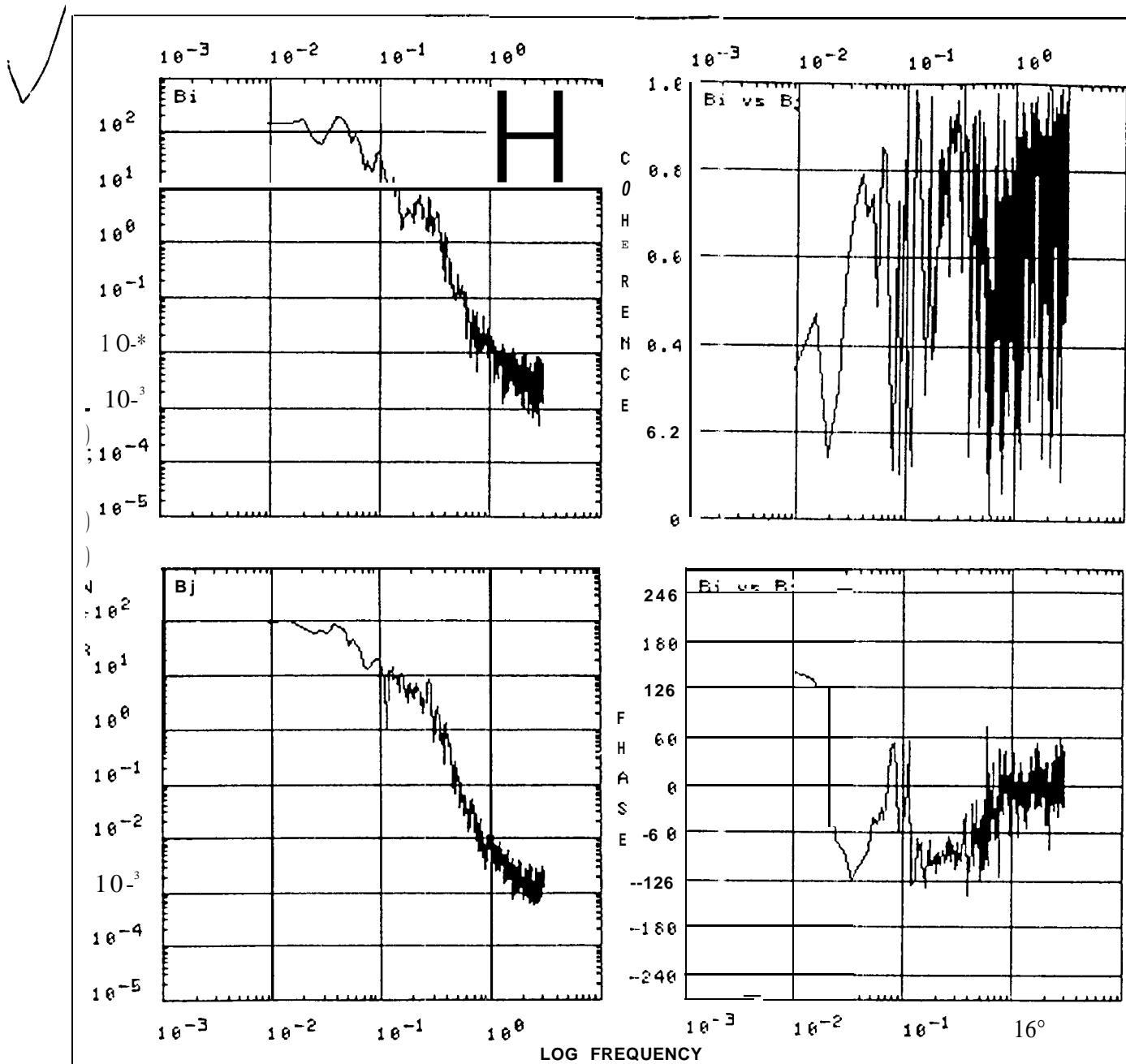
Frequency Bands: 633   Bands Averaged: 3
Bandwidth(Hz) : 0.0048088 Resolution(sec): 0.164
Start: 83 290 OCT 17 01:03:44.881
Stop :   83 290 OCT 17 01:07:15.954

Figure 24

ISEE-3

Day 290, 1983

0113:29.12-0113:56.60

R. H./L.H. Mixed $\otimes B_0$ $\theta_{BK} = 34°$
$\theta_{XK} = 13°$
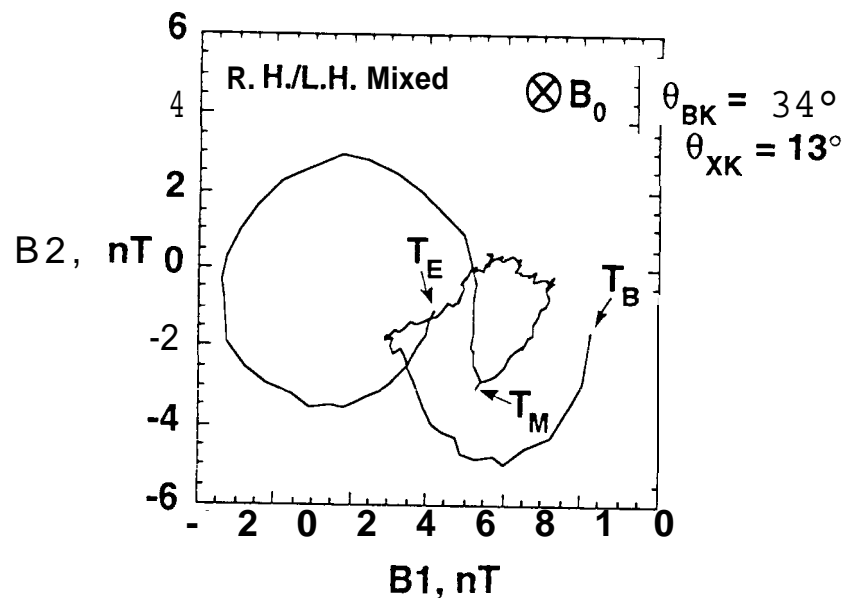
$T_B = 0113:29.12$

$T_M = 0113:49.78$

$T_E = 0113:56.60$

0113:29.12-0113:49.78

R "H" $\otimes B_0$ $\theta_{BK} = 38°$
$\theta_{'K} = 14°$
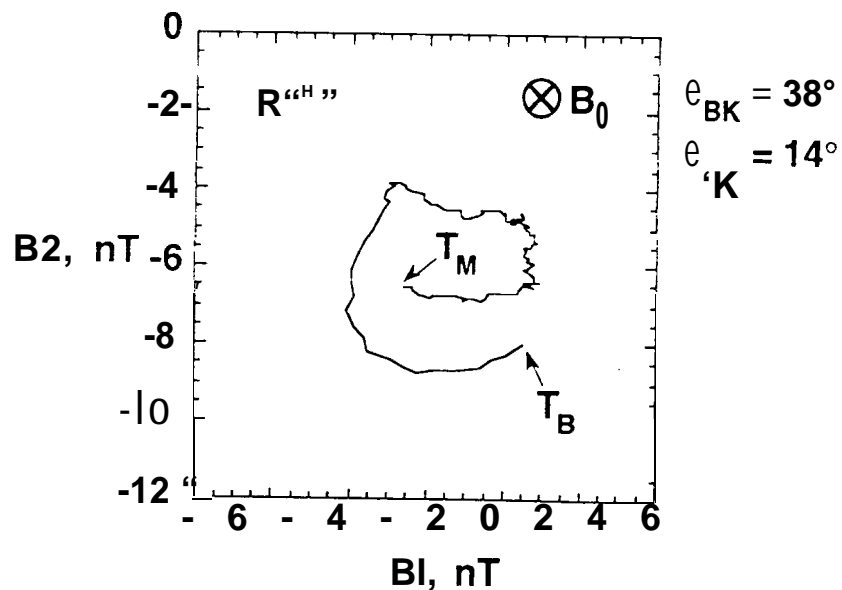
0113:49.78-0113:56.60

L.H. $\otimes B_0$ $\theta_{BK} = 21°$
$\hat{\theta}_{XK} = 26°$
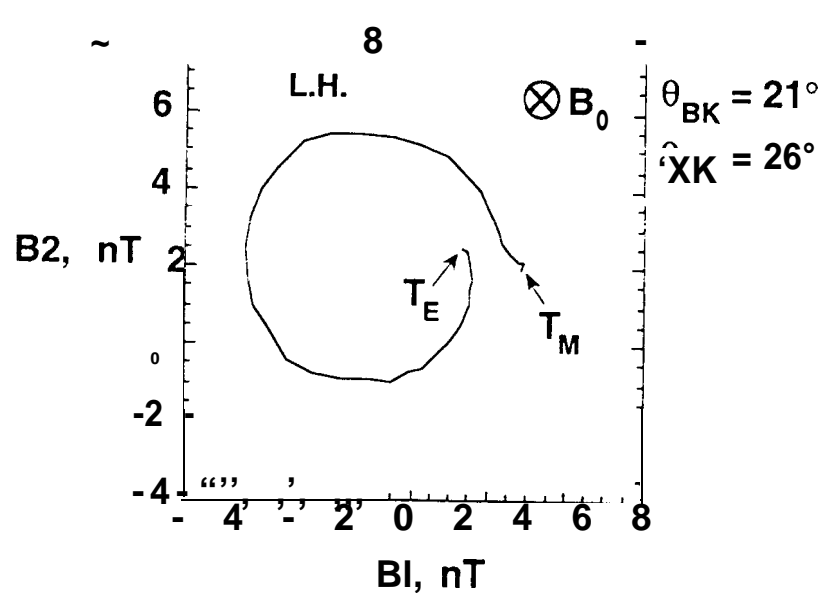
Figure 25

TANGENTIAL DISCONTINUITY

$$\vec{B_1} \cdot \hat{c} = \vec{B_2} \cdot \hat{c} = 0$$

SIDE 1

SIDE 2

$\vec{B_2}$

$\vec{B_1}$

$\Delta \vec{B}$

$\hat{n}$
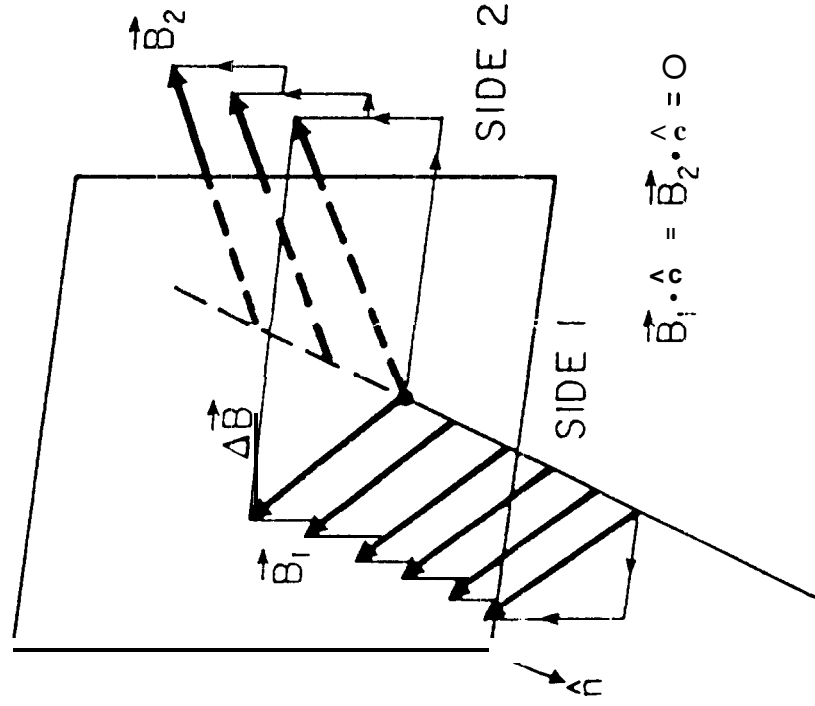
ROTATIONAL DISCONTINUITY

$$\vec{B_1} \cdot \hat{n} = \vec{B_2} \cdot \hat{n} \neq 0$$

$$|\vec{B_1}| = |\vec{B_2}|$$

SIDE 1

SIDE 2

$\vec{B_2}$

$\vec{B_1}$

$\hat{n}$
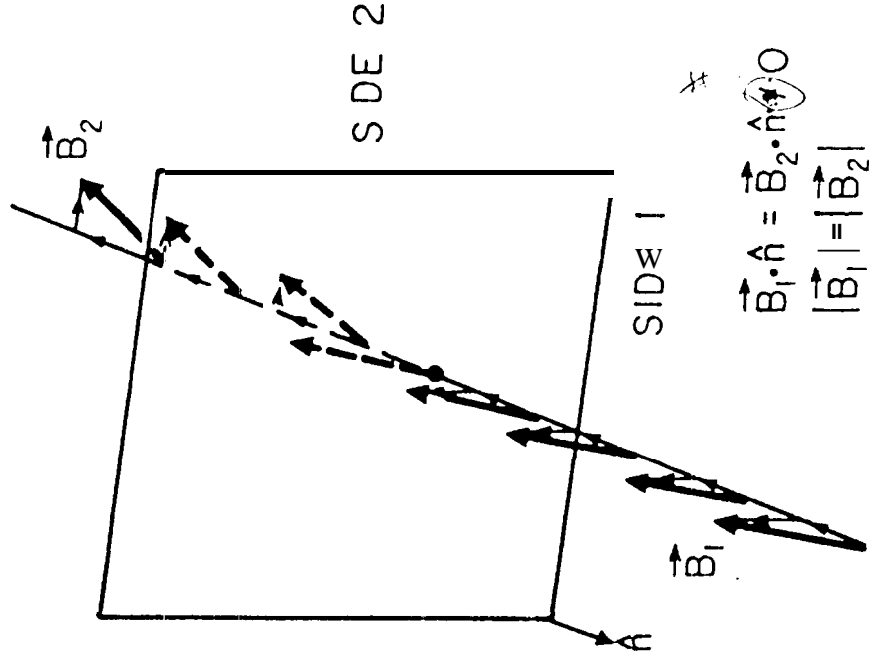
Figure 26

ROTATIONAL DISCONTINUITY

PIONEER 10 DAY 136, 9 2 I AU
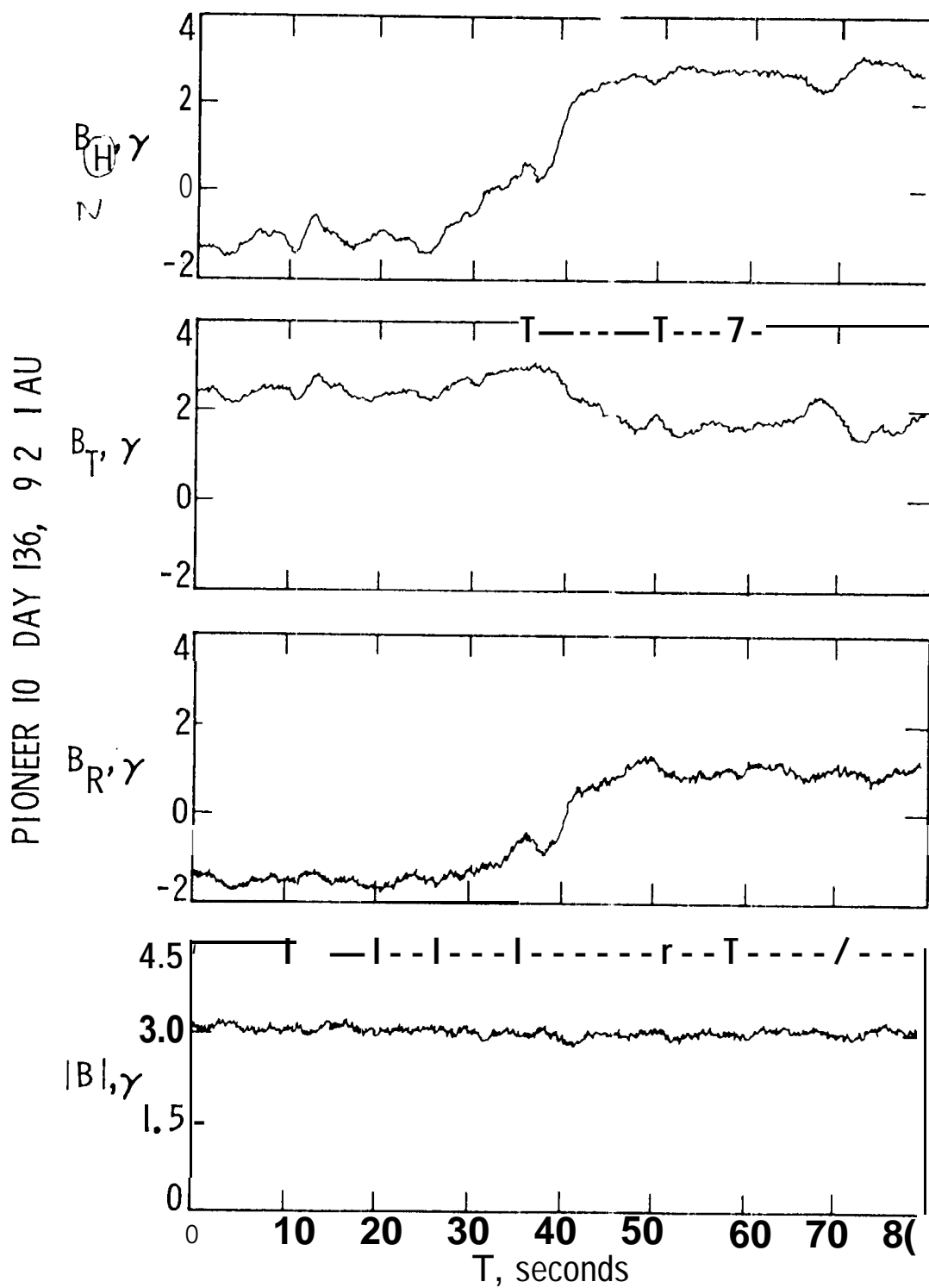
Figure 27

ROTATIONAL DISCONTINUITY

PIONEER 10
DAY 136, 1972
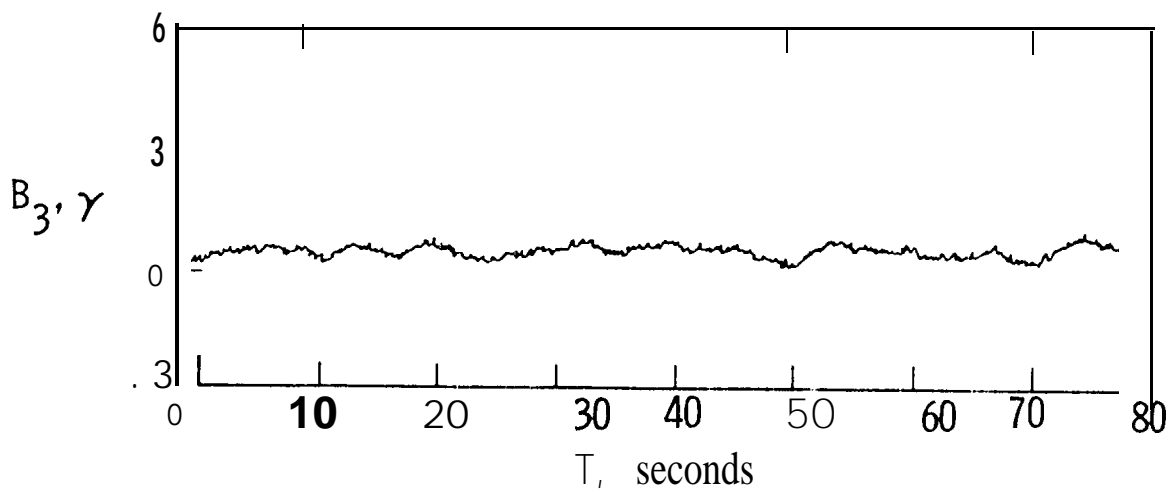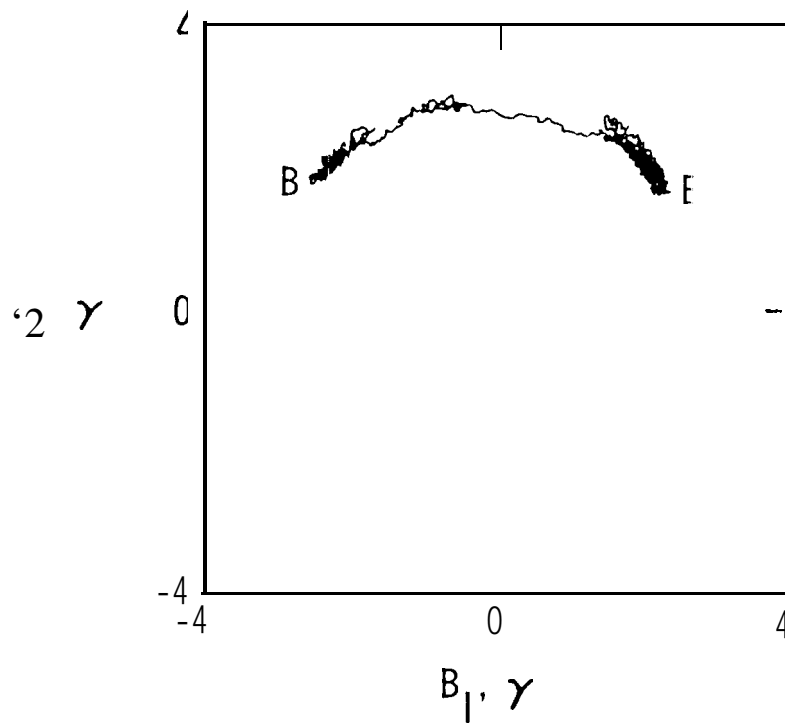
Figure 28

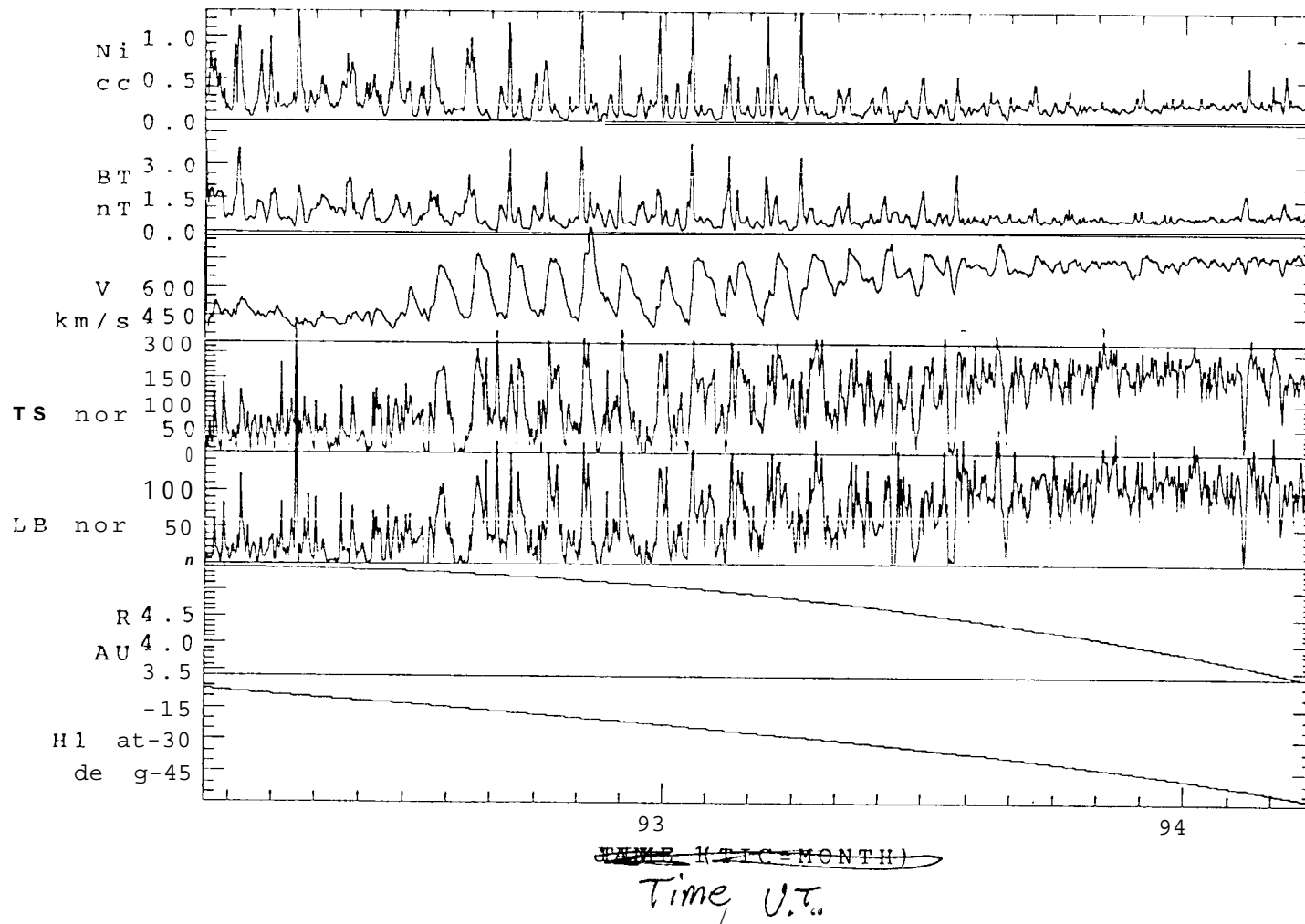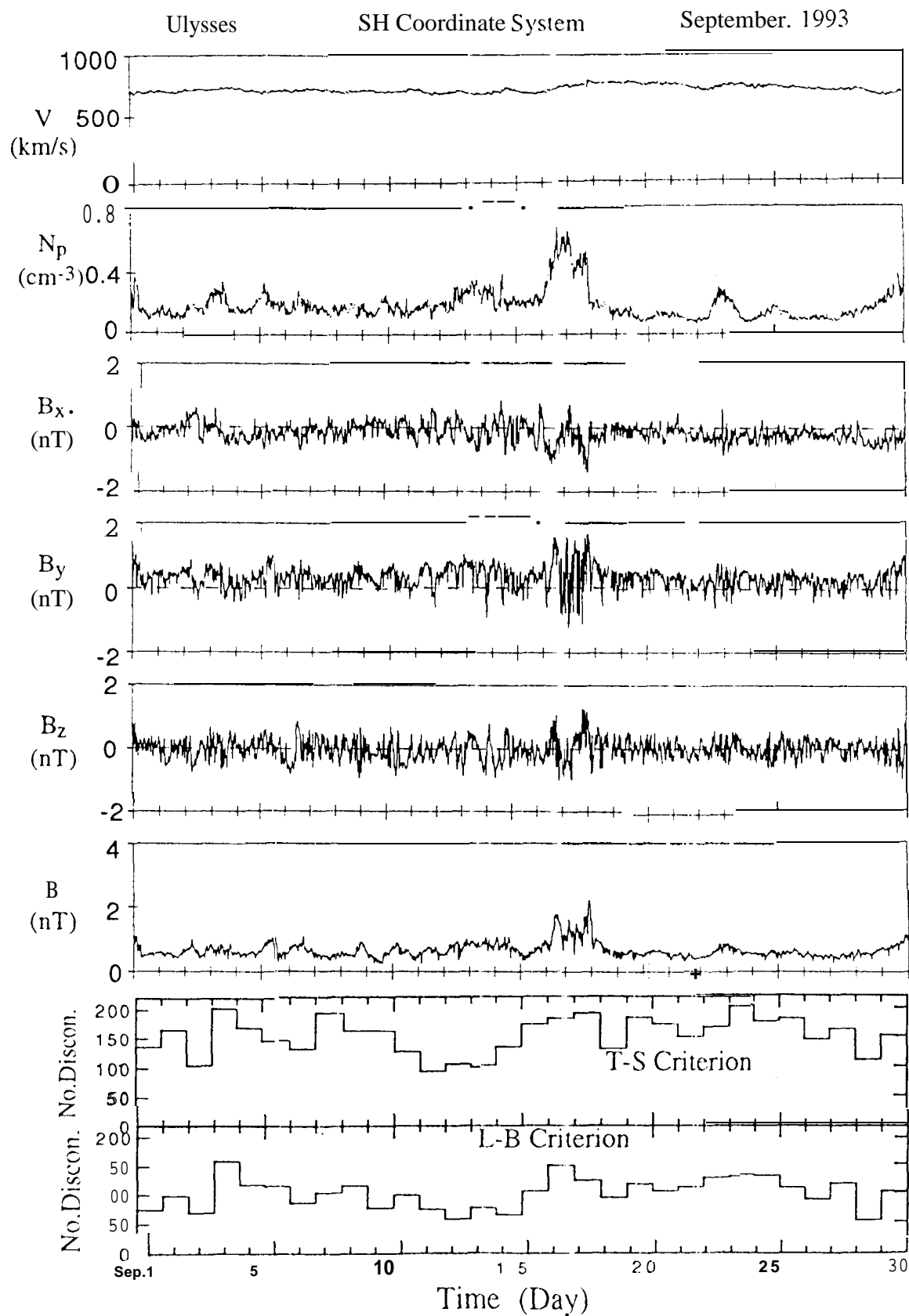# Ulysses out of the ecliptic plane after the Jupiter encounter

Figure 29

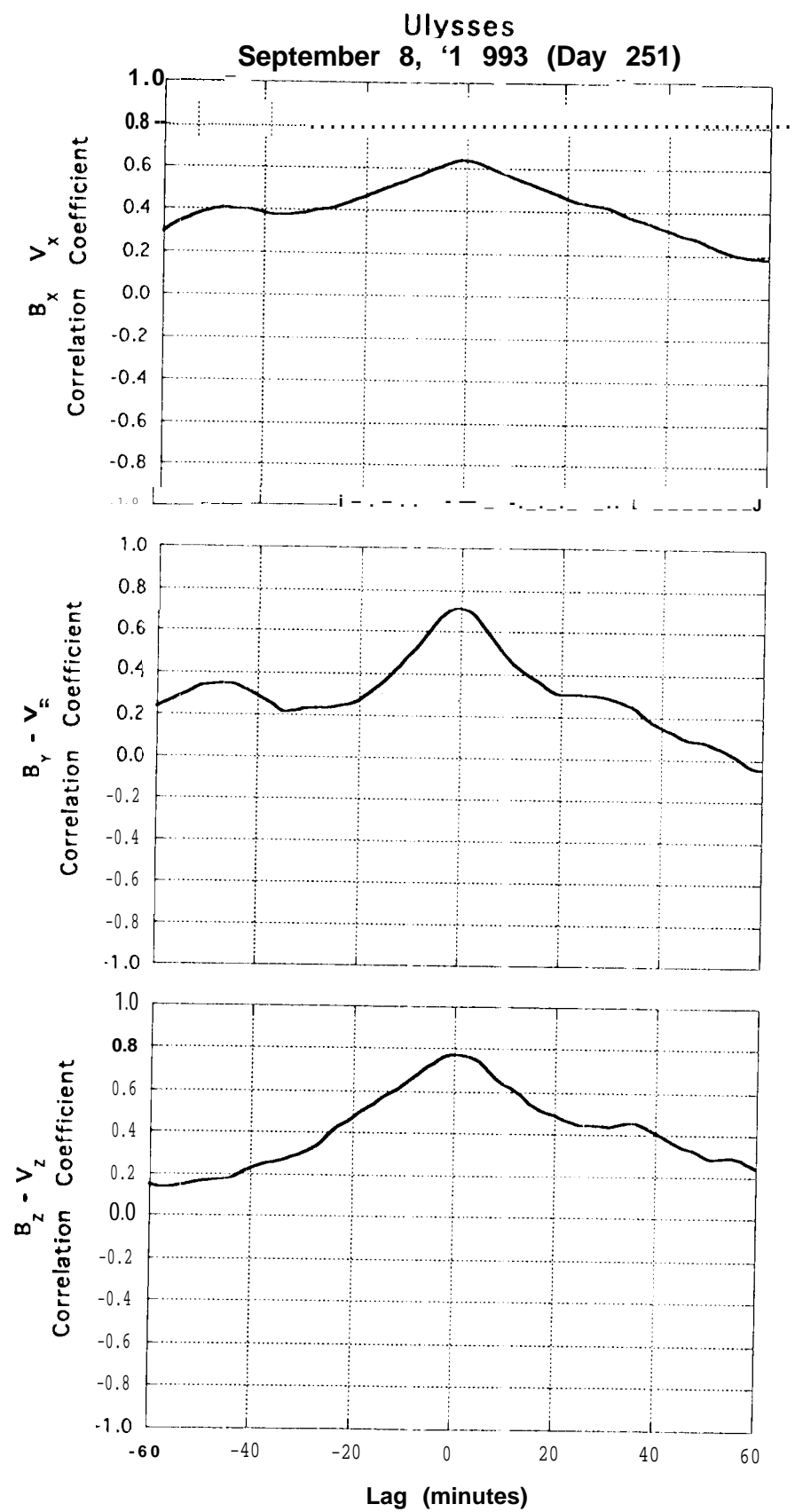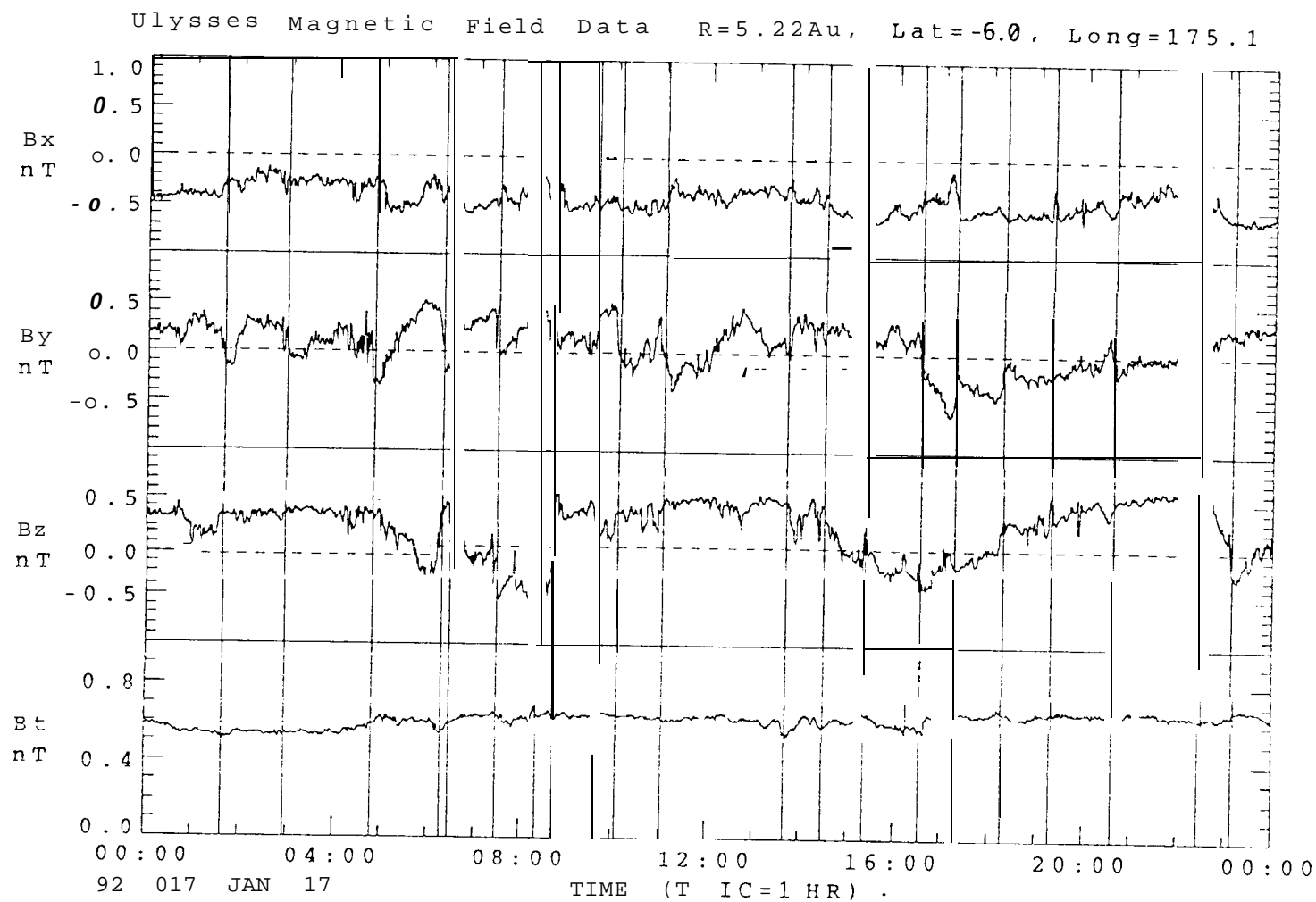Ulysses   SH Coordinate System   September. 1993

Time (Day)

Figure 30

Ulysses
September 8, '1 993 (Day 251)

Figure 31

Figure 32

ULYSSES

January 17, 1992
Day 17

Wave + Discontinuity
0508 - 0622 UT

Discontinuity interval
0614 - 0622 UT

Wave interval
0508 - 0614 UT

Figure 33
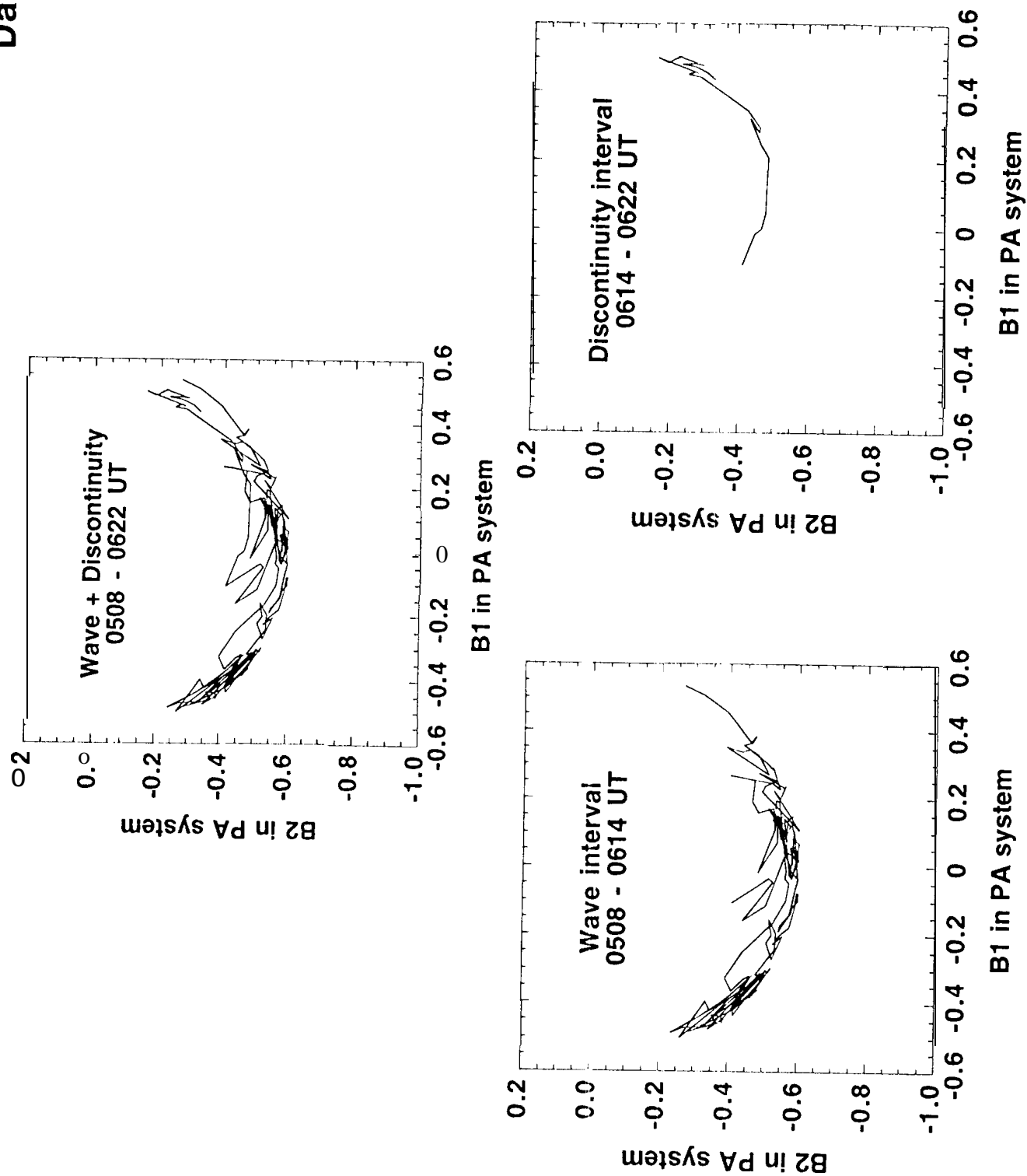
TYPE OF DISCONTINUITY	MASS FLUX P_n	CHANGE IN MAGNETIC FIELD $[\vec{H}]$	
CONTACT D SCONTINUITY	0	$[\vec{H}_t] = 0$	$H_n \# 0$
TANGENTIAL DISCONTINUITY	0	$[\vec{H}_t] \neq 0$	$H_n = 0$
ROTATIONAL DISCONTINUITY	$\neq 0$	$[H_t]'0$	$H_n \neq 0$
SHOCK	$\#0$	$[\vec{H}_t] \neq 0$ $[H_t] \neq 0$	$H_n \neq 0$

Table 1